Universiteit Utrecht

Opleiding Natuur- en Sterrenkunde &
UCU Liberal Arts and Sciences

Numerical Modelling of Indium Arsenide Chains and Lattices

Bachelor Thesis

August Joan Otto Röell

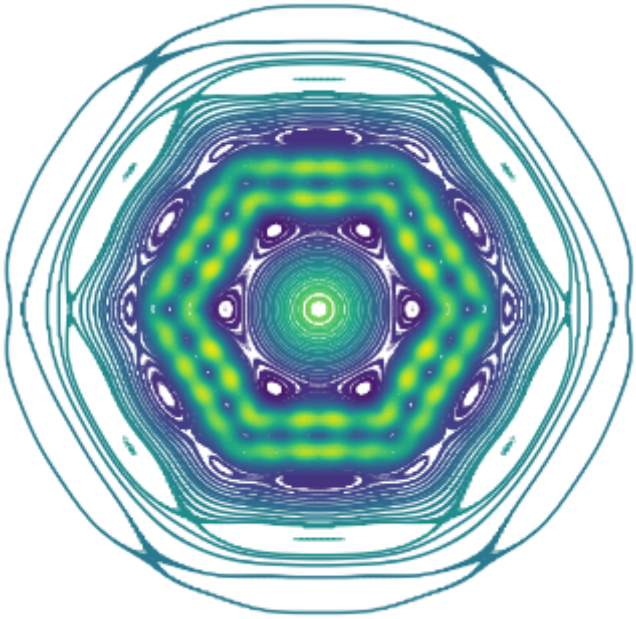

Supervisors:

Prof. Dr. C. Morais Smith
ITF

MSc J. van den Broeke
ITF

03/07/2020

Acknowledgements

I would like to take this opportunity to thank Jette, Cristiane, and the entire condensed matter systems group for the many inspiring talks and discussions.

The front page image is a contour plot of the local density of states at high energy for a system with a hexagonal potential, plotted in real space. The image was made using the code developed in this thesis. The image shows both hexagonal and circular symmetry, indicating that the hexagonal potential can be treated as a perturbation on a circular potential, as will be substantiated in this thesis.

Contents

1 Introduction **1**

2 Overview of the Field of Research **2**
2.1 Carbon Monoxide on Copper 2
2.2 Patterned Arsenic Compounds 7
2.3 Potassium Atoms Trapped by Lasers 8
2.4 STM patterned Indium Arsenide 9

3 Numerical Methods **11**
3.1 Functions and Libraries 11
3.2 Modelling of one-dimensional systems 12
3.3 Modelling of two-dimensional systems 15
3.4 Lorentzian Broadening and the Local Density of States 18
3.5 Stripping functions 19

4 Results **23**
4.1 One-dimensional simulations 23
4.2 Two-dimensional Simulations 26
4.3 Modelling of the Indium Arsenide Chain 30
4.4 Modelling of Hexagonal Quantum Rings 37

5 Conclusion **58**

1 Introduction

The discovery and isolation of graphene in 2014, by Andre Geim and Konstantin Novoselov [21], had a profound influence in condensed-matter physics. Graphene, an allotrope of carbon, and a remarkably perfect realization of a two-dimensional material, is a one-atom-thick electron system consisting of carbon atoms on a honeycomb lattice. With the subsequent discovery of massless Dirac fermions in graphene [22], interesting new avenues into the study of quantum electrodynamics, which until then was restricted to high-energy physics, have been opened up ([1], p. 1)([25], p. 625)([22], p. 197).

The intriguing properties of graphene are, however, not restricted to real graphene alone. Researchers have shown analogous properties in a number of artificial systems with sixfold symmetry, ranging from molecules on copper [7] [8] [10] [14] [25] [26] [29], to atoms trapped in crystals of light [5] [4] [25] [26] [31], and further to patterned semiconductor structures [12] [24] [25] [26] [32]. These 'artificial graphene' systems, however different from each other, share the quality that their structure is far more pliable than that of real graphene. As artificial systems, their properties can be tuned in ways that are impossible in real graphene. This makes the artificial graphene structures ideal candidates to study the exciting properties of graphene and other honeycomb lattice materials ([25], p. 625)([26], p. 422-423).

Due to the size and complexity of these artificial systems, particularly when studying deviations from the perfect honeycomb lattice, complete analytical treatment is often unfeasible. On the other hand, experimental research, though without a doubt ultimately necessary, is not only prone to all kinds of error, but can also be time and resource consuming. Developing numerical methods that can produce approximate solutions for quantum systems, like the artificial graphenes, can aid the detection of interesting behaviours, and is a time- and resource-efficient way of studying these systems. Approximate numerical methods are a powerful addition to both the analytical and empirical study of the promising new artificial graphene materials ([3], p. 714).

In this thesis, we develop a number of numerical methods to model one- and two-dimensional, non-interacting, electron systems with arbitrary potentials in the Python programming language. These methods are then tested on a number of well-known systems in order to verify whether the code runs as expected. Finally, using the numerical methods developed here, we model a number of scanning tunneling microscope (STM) patterned indium arsenide structures, which, like the other patterned semiconductor structures mentioned above, can be used to create artificial graphene systems. The ambition of this thesis is to develop a set of numerical methods that can successfully model STM patterned indium arsenide structures, and particularly those with slight deviations from the perfect honeycomb lattice.

2 Overview of the Field of Research

In the endeavour to study the behaviour of electrons in graphene, a number of different artificial lattices mimicking the honeycomb structure of graphene have been proposed and studied. Three such honeycomb lattices, ranging over length scales of just a few nanometres to multiple millimeters, will be discussed here in more detail, in order to contextualize and introduce the artificial lattice studied in this work, namely STM patterned indium arsenide.

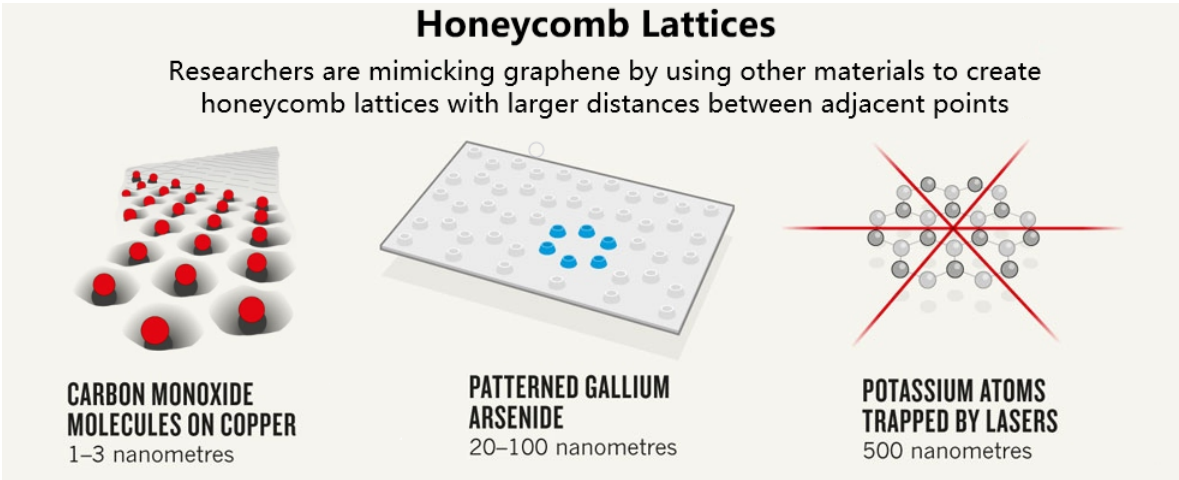

Figure 1: Overview of several artificial, graphene-like lattices, as adapted from Reich [26].

2.1 Carbon Monoxide on Copper

Some of the smallest graphene-like artificial lattices to date are constructed by manipulating the positions of carbon monoxide molecules over a copper surface, as described in Gomes et al. [10]. In particular, carbon monoxide molecules are adsorbed on the surface of a clean copper Cu(111) surface, after which the positions of the carbon monoxide molecules are manipulated individually using the tip of an STM. Here, (111) are the Miller indices describing the lattice plane that the Cu(111) surface follows. As this artificial graphene consists of carbon monoxide molecules, the system is also referred to as *molecular graphene*. By manipulating the constituents of the artificial lattice individually at the atomic level, graphene-like lattices can be constructed at the scale of just a few nanometres ([10], p. 306)([26], pp. 422-423).

One of the reasons Cu(111) is chosen as the surface for the carbon monoxide molecules to be adsorbed on is the property of the ground-state electron system on the Cu(111) surface. Copper has a face-centered cubic crystal structure. The lattice plane described by the Miller indices (111) in such a cubic crystal is depicted in figure 2. The electron system on a Cu(111) surface has the property that, above a certain energy, it is very localised to the surface, rather than to the bulk of the material. Because of this, the electron system can effectively be treated as a two-dimensional electron system. Moreover, since copper is a good conductor, the electron system on the Cu(111) surface is almost free. Therefore, any property of molecular graphene will be due, predominantly, to the arrangement of the carbon monoxide molecules, rather than the copper background ([10], p. 306) ([33], pp. 663, 665).

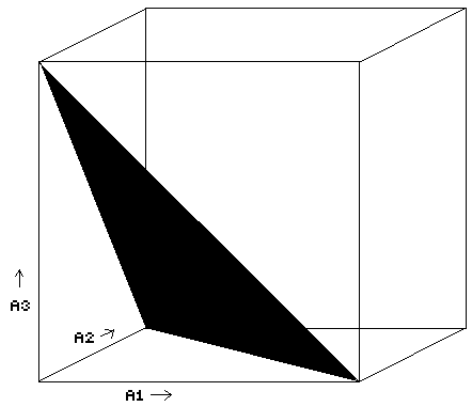

Figure 2: Plane with Miller indices (111) in a cubic crystal.

Arranging the negatively charged carbon monoxide molecules adsorbed on the Cu(111) surface in a triangular lattice shape, which is the anti-lattice of the honeycomb lattice, forces the electrons in the two-dimensional electron system to form a honeycomb pattern. Since the setup of molecular graphene allows for exceptional control over the positions of the carbon monoxide molecules through the use of an STM, a perfect electronic honeycomb lattice can be constructed at the scale of several nanometres. An image of such an artificial honeycomb lattice is given in figure 3, as found in Gomes et al. [10]. For this picture, 149 carbon monoxide molecules were arranged so that their positions, as seen in figure 3, correspond to the dark centers of the hexagons in the honeycomb lattice. Moreover, since the carbon monoxide molecules are negatively charged, a repulsive barrier around the lattice is needed, to constrain the electrons to the molecular graphene system. In order to minimize the thermal fluctuations of the system, the sample is cooled to 4.2 K. The spacing between individual carbon monoxide molecules can only take certain values, since the adsorption sites of the Cu(111) surface dictate which arrangements of adsorbed carbon monoxide are possible. In the case of figure 3, the spacing between the carbon monoxide molecules is the square root of three, times the lattice constant of the Cu(111) surface, so that $d = \sqrt{3}a = 1.92$ nm.

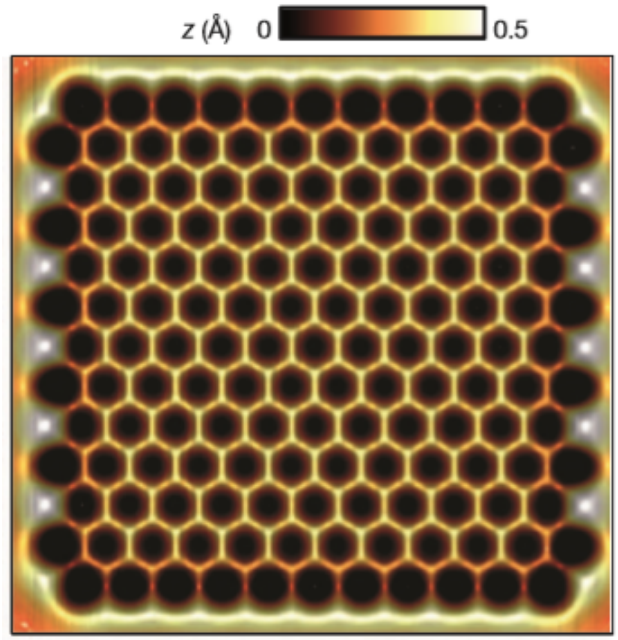

Figure 3: Artificial honeycomb lattice formed through triangular arrangement of negatively charged carbon monoxide molecules, as found in Gomes et al. [10].

Using an STM, the differential tunneling conductance at a given position in the artificial lattice can be measured. This differential tunneling conductance for molecular graphene can then be divided by the spatially averaged value for the differential tunneling conductance of the Cu(111) surface. Normalizing the results in this way removes the featureless slope that is present in the conductance spectrum of Copper, and is meant to prevent any unwanted noise that could arise from interactions between the Cu(111) surface and different STM tips. The ratio of the measurements and the differential tunneling conductance of the copper surface is the normalized differential conductance spectrum, $\tilde{g}(\tilde{E}, \vec{r})$, which, in all cases treated here, is directly proportional to the local density of states of the artificial lattice under consideration. The tilde is used to indicate that the quantity under consideration is a continuum property of the fermions ([2], pp. 5-6)([10], p. 307).

Plotting $\tilde{g}(\tilde{E}, \vec{r})$ against the energy $\tilde{E}$ of the fermionic particles in the molecular graphene system, as in figure 4, reveals a linear dispersion that is the characteristic of a Dirac cone, just as in real graphene. In particular, $\tilde{g}(\tilde{E}, \vec{r})$ is measured over the sublattices defined by positions A and B, as indicated in the inset. The spatially averaged measurements over sublattice A are given by the filled circles, while those over sublattice B are given by the open circles ([10], p. 307).

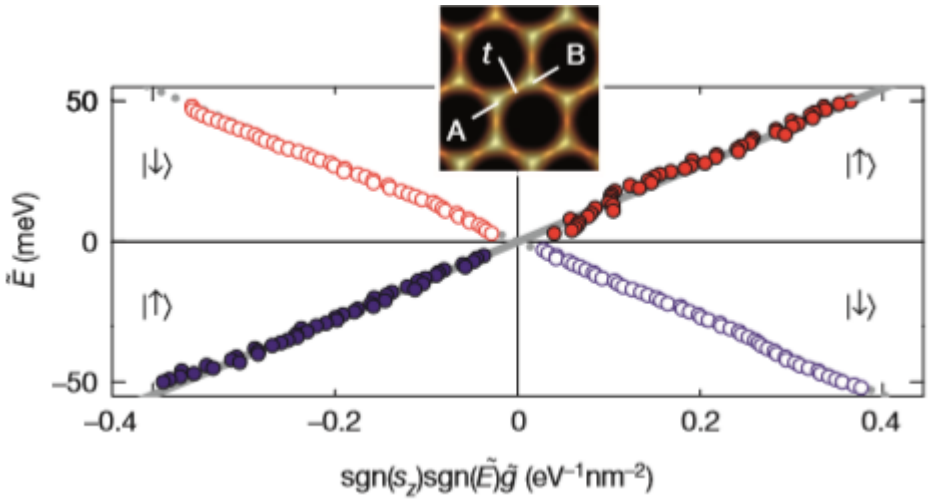

Figure 4: Linearly dispersing fermionic particles in molecular graphene, as found in Gomes et al. [10].

Notice that, near the Dirac point, no measurements are reported. In this region, the energy obeys $|\tilde{E}| < eV_{rms}$, where V_{rms} is the modulation voltage of the STM. At such low energies, instrumental broadening becomes too large to allow for accurate measurements ([10], p. 307).

In general, the differential conductance spectrum of the molecular graphene system agrees qualitatively with the conductance spectrum of real graphene. The conductance spectra are compared in figure 5. Sub-figure 5a is adapted from Gomes et al. [10], and sub-figure 5b is taken from Hobson and Nierenberg [11].

In the case of molecular graphene, the differential conductance spectrum is measured over different positions in the artificial lattice using an STM, after which the spatial average of these measurements is normalized by dividing it by the spatially averaged differential conductance spectrum of a clean Cu(111) surface. The resulting normalized, spatially averaged differential conductance spectrum of molecular graphene is plotted in green in figure 5a. The accompanying dashed plot is a tight-binding calculation for the molecular graphene system ([10], p. 307).

The conductance spectrum of molecular graphene, measured in this way, can be compared to the conductance spectrum of real graphene. The first analytical treatment of the conductance spectrum of graphene, assuming only nearest neighbor hopping, can be found in Hobson and Nierenberg [11]. The conductance spectrum in figure 5b is the numerically determined conductance spectrum for graphene, as found in Laughlin [17].

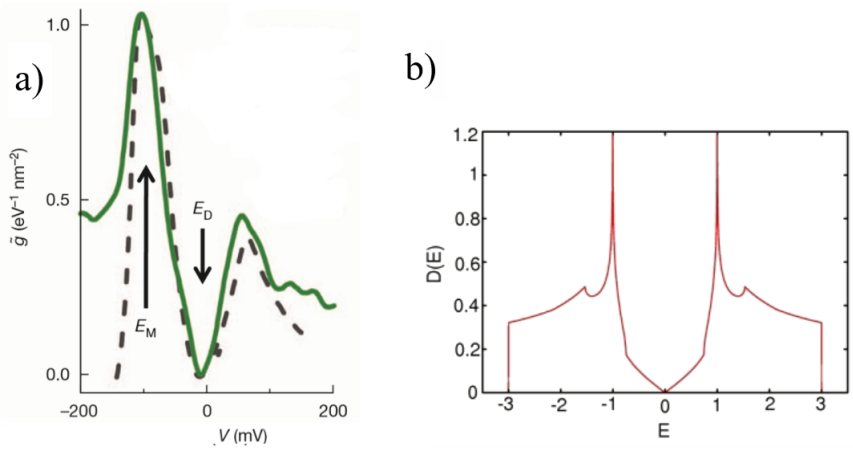

Figure 5: **a)** Normalized, spatially averaged differential conductance spectrum of molecular graphene (solid green line) and an accompanying tight-binding calculation for the same system (dashed black line). Figure adapted from Gomes et al. [10].
b) Numerical solution for the conductance spectrum of graphene. Figure found in Laughlin [17].

The key advantages of molecular graphene as a lattice-lookalike of real graphene are the remarkable precision and control achieved when individual carbon monoxide molecules are positioned on the Cu(111) surface using the tip of an STM. As can be seen from figures 3, 4, and 5, molecular graphene, constructed in such a way, mimics the behaviour of real graphene well ([10], pp. 306, 310).

A serious drawback of the setup, however, is the amount of scattering to the bulk, which adds to the lifetime broadening of the electrons, and in turn to a broadening of $\tilde{g}$. This broadening can clearly be seen when comparing figures 5a and 5b ([10], p. 308).

The two-dimensional electron system on a pure Cu(111) surface is usually decoupled from the bulk electrons. However, when the binding energy of the surface electrons approaches the Fermi level, the surface state approaches the bulk continuum. This causes an increasing delocalization into the bulk and, consequently, an enhanced coupling to the bulk states. The energy dispersion relation of the surface state of pure Cu(111), as well as that of the bulk continuum of states, can be seen in figure 6, as found in Kevan [15]. The bulk continuum is calculated assuming a parabolic fit to Fermi surface data. The figure shows that, just above the Fermi level, the surface state enters the bulk continuum ([15], pp. 526, 527, 529).

By adsorbing negatively charged carbon monoxide molecules on the Cu(111) surface, the potential on the surface is raised, which increases the binding energy of the surface state electrons. In this way, the broadening of $\tilde{g}$, as reported by Gomes et al. [10], which is larger than the broadening observed in pure copper, can be explained by the presence of the adsorbed carbon monoxide molecules on the Cu(111) surface that make up the molecular graphene ([10], p. 308).

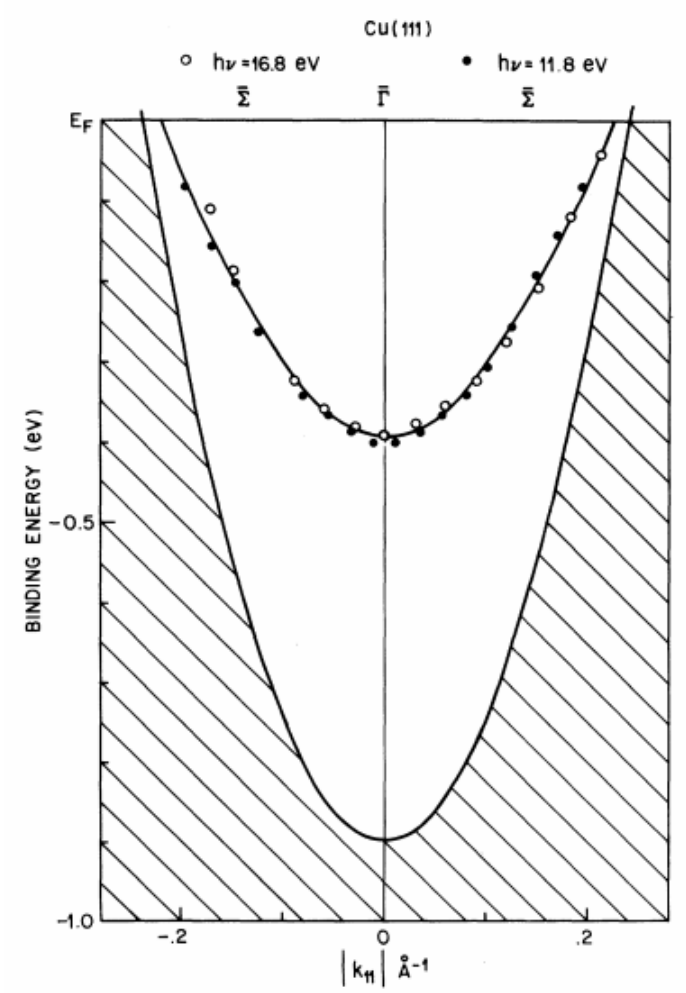

Figure 6: The energy dispersion relation of the surface state of pure Cu(111), as found in Kevan [15], measured using photoemission spectrometry. Measurements using incident photons of energy $h\nu = 16.8$ eV are shown using the empty circles, while measurements using photons of energy $h\nu = 11.8$ eV are shown using the filled circles. A parabolic least squares fit is supplied, and the shaded region is the projected bulk continuum of states.

2.2 Patterned Arsenic Compounds

An alternative approach to producing artificial hexagonal lattices is the creation of patterned arsenic compounds, such as gallium or indium arsenide. Both gallium and indium arsenide are type III-V semiconductor materials, which makes them very suitable for conventional top-down nanofabrication approaches. Type III-V semiconductor materials are composite semiconductors, consisting of two chemical elements, one of which donates three electrons, while the other donates five. In the case of gallium or indium arsenide, it is the gallium, respectively indium, that donates three electrons, while the arsenic donates five. Using these nanofabrication techniques, gallium and indium arsenide materials can be created that consist of orders of magnitude more particles than any of the other artificial lattice approaches are capable of. It is this scalability that makes patterned arsenic compound arti-

ficial lattices suitable for the studying of long-range interactions, many-body effects, as well as spin-orbit interactions ([25], p. 625) ([32], p. 1).

Other advantages of arsenic compounds are connected to their material properties. When comparing semiconductors, like gallium and indium arsenide, to metals, like copper, semiconductor materials show significantly less screening effects, which may reduce the scattering to the bulk described in section 2.1. Moreover, the semiconductor arsenic compounds are characterised by much less contamination than real graphene. It is possible that charged impurities that are trapped either between the graphene surface and the underlying substrate, or on top of the graphene surface, play a role in reducing the mobility of graphene. Being able to produce artificial lattices with very little contamination would offer a natural solution to this problem ([9], p. 3)([24], p. 4).

However, a major drawback of arsenic compounds, patterned using top-down nanofabrication approaches, is the amount of structural disorder in the system. The other artificial lattice approaches either show no structural disorder at all (see section 2.3), or are characterised by tunneling energy scales that are much larger than the structural disorder of the system (see section 2.1) ([25], p. 625) ([32], p. 1).

2.3 Potassium Atoms Trapped by Lasers

A radically different approach to creating an artificial graphene lattice is offered by trapping ultra-cold potassium atoms in a honeycomb optical lattice. Using a setup of interfering laser beams, a highly tunable periodic potential can be created, which affects an ultra-cold gas of fermionic ^{40}K atoms. An image of the optical honeycomb lattice is given in figure 7, as found in Tarruell et al. ([25], p. 625)([31], p. 302).

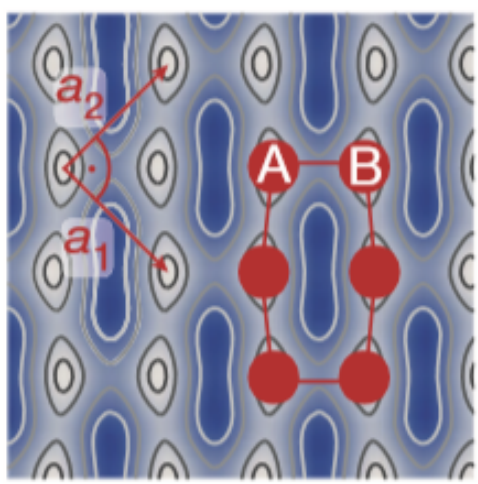

Figure 7: Contour plot of the real-space potential of the optical honeycomb lattice, as found in Tarruell et al. [31]. White regions correspond to lower potential energy, while blue regions indicate higher potential energy, and the sublattices are indicated by 'A' and 'B'.

Just like electrons, ^{40}K atoms are fermionic particles, which is why ultra cold potassium atoms are suited for creating artificial graphene lattices. Optical lattices with bosonic ^{87}Rb

species have also been realized, as described in Lühmann et al. [19] and Di Liberto et al. [4].

In solids, it is the rigid structure of the material that determines the mass and velocity of the electrons in the system. By using a periodic potential of interfering laser beams, the structure of the system becomes very flexible and tunable, which in turn allows the cold atoms in the optical lattice to be pushed into regimes that are nearly or fully unattainable in real graphene. By offering control over the nature, strength, and range of inter-particle interactions, ultra-cold potassium atoms in optical lattices can be used to study regimes such as ultrastrong spin-orbit coupling and non-Abelian gauge fields ([25], p. 625, 629)([31], p. 302).

2.4 STM patterned Indium Arsenide

The artificial lattice considered in this work, is a system consisting of indium atoms, each placed individually using an STM, on a indium arsenide surface. In particular, indium atoms of charge +1e are individually placed and adsorbed on a InAs(111)A surface, where the '(111)' designates the Miller indices (see figure 2), and the 'A' indicates the surface is indium-terminated. The indium atoms that are adsorbed on the InAs(111)A surface will be referred to as adatoms. An experimental realization of a linear chain of indium adatoms on the InAs(111)A surface is shown in figure 8.

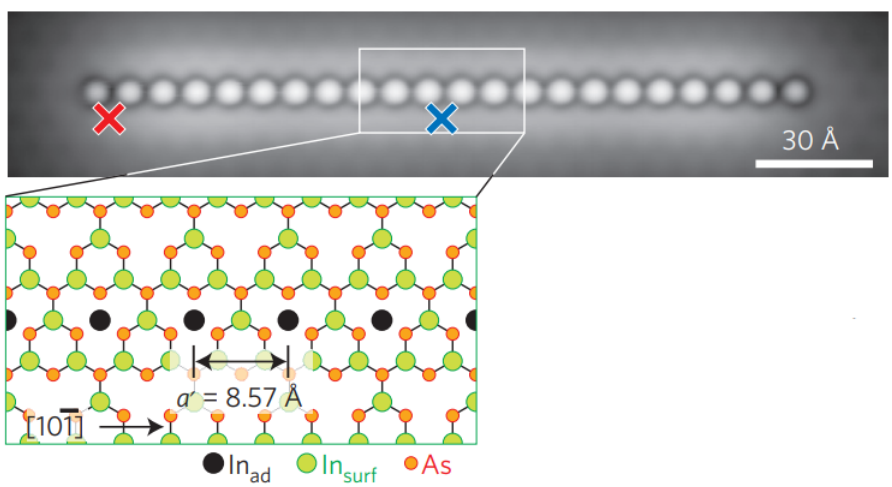

Figure 8: An STM topography image of a linear chain of indium adatoms on the InAs(111)A surface, including a schematic zoom, showing the structure of the InAs(111)A surface, and the positions of the adsorbed indium adatoms. Figure from Fölsch et al [6].

The STM patterned indium arsenide artificial lattice is, in many ways, a hybrid between the molecular graphene [10], discussed in section 2.1, and the patterned arsenic compounds, discussed in section 2.2. In terms of material properties, STM patterned indium arsenide falls in the category of arsenic compounds. Indium arsenide is a type III-V semiconductor, with significantly less screening effects than the copper surface in molecular graphene, and it can be made with much less contamination than real graphene ([9], p. 3)([24], p. 4).

In terms of production method, however, STM patterned indium arsenide closely resembles molecular graphene [10]. By making use of an STM to place each indium adatom individually, the same level of precision and control can be achieved as for carbon monoxide on copper. This deals with the current problem of structural disorder in patterned arsenic compounds. A notable difference between the production methods of STM patterned indium arsenide and molecular graphene is that, due to the indium adatoms being positively charged, no repulsive barrier is needed around STM patterned indium arsenide structures. ([24], p. 4).

It should be noted that, though adopting the STM patterning technique solves the structural disorder problem and allows for superior precision and control, the STM patterned indium arsenide no longer has the superior scalability of the top-down nanofabricated arsenic compounds. By using STM patterning, instead of top-down nanofabrication, the STM patterned indium arsenide artificial lattice is a choice of quality over quantity.

Ideally, there will be techniques developed to create high quality artificial lattice in the quantities needed, not only to use in research, but to be used in potential applications as well. Top-down nanofabricated arsenic compounds show promise in this respect, and STM patterned indium arsenide can be used to probe the properties of these materials right now ([9], p. 1)([24], p. 4)([25], pp. 625-627, 631).

3 Numerical Methods

"The underlying physical laws necessary for the mathematical theory of a large part of physics and the whole of chemistry are thus completely known, and the difficulty is only that the exact application of these laws leads to equations much too complicated to be soluble. It therefore becomes desirable that approximate practical methods of applying quantum mechanics should be developed, which can lead to an explanation of the main features of complex atomic systems without too much computation."

– P.A.M. Dirac

In the spirit of Paul Dirac's quote above, this section seeks to develop a number of numerical methods that open up complex quantum mechanical problems to approximate treatment using the computational power of modern computers.

All of quantum mechanics, in one way or another, is related to the Schrödinger equation, which, in its most general form, is given by equation (1). However, if complex quantum mechanical problems are to be made accessible to numerical treatment, suitable approximations to the general, time-dependent, Schrödinger equation are needed.

$$i\hbar\frac{d}{dt}\left|\Psi(t)\right\rangle = \hat{H}\left|\Psi(t)\right\rangle . \tag{1}$$

The first simplification of the eigenfunction problem posed by equation (1), is that all numerical methods will be restricted to finding stationary states, instead of general wave functions. Stationary states are wave functions for which all observable properties, such as energy and probability density, are time-independent. This simplification is reasonable, as the systems that will be studied are assumed to be static, so that their properties can be described by stationary states. In this way, the general, time-dependent, Schrödinger equation reduces to the general, time-independent, Schrödinger equation

$$\hat{H}\left|\psi\right\rangle = E\left|\psi\right\rangle . \tag{2}$$

Moreover, assuming all particles move at non-relativistic speeds, the Hamiltonian can be rewritten, giving the non-relativistic, time-independent, Schrödinger equation

$$\left[\frac{-\hbar^2}{2m}\nabla^2 + U(\vec{r})\right]\psi(\vec{r}) = E\psi(\vec{r}). \tag{3}$$

However, the non-relativistic, time-independent, Schrödinger equation remains an analytic equation that is not immediately open to numerical analysis. Therefore, equation (3) has to be transformed into a problem that is open to numerical treatment, while staying as close to the original as possible. This is the topic of sections 3.2 and 3.3.

3.1 Functions and Libraries

In this project we utilize a number of functions. Some of these were written by myself, and others were imported from pre-designed python libraries. For completion sake, the exact libraries are described below, but knowledge of these libraries is in no way required for a

general understanding of the project. Someone looking for a general understanding of the methods can skip the following paragraph.

The code for the numerical simulations of this thesis project makes use of three python 3.8.1 modules. For the creation of evenly spaced intervals and meshes, as well as element-wise addition and multiplication of one-dimensional arrays, the numpy 1.6.1 library is used. The numerical methods utilize the *scipy.sparse* module of scipy 1.5.0, which helps in keeping the operations on large sparse two-dimensional arrays tractable. In particular, the *scipy.sparse.linalg.eigsh* function, as based on the ARPACK library of Fortran 77, is helpful to the program. Finally, matplotlib 3.1.3 is used to visualize the obtained data. For the three-dimensional plots, the *mpl_toolkits.mplot3d* module from matplotlib 2.0.2 is used.

3.2 Modelling of one-dimensional systems

As a first enterprise, we numerically solve the Schrödinger equation (3) for a single, non-relativistic, electron in a one-dimensional box, subject to an arbitrary potential $U(x)$ over the interval of the box.

As we seek to solve for such a system using numerical computation methods, we must define our system in a way that is open to numerical analysis. The system we apply numerical methods to must have a finite number of coordinate points, as opposed to a continuous system with an infinite number of coordinate points. In other words, we must approximate the system we wish to model by a discretisation with a finite resolution.

In our code, we therefore start off by defining the parameters that specify our system, such as the length (L) of our box and the resolution (N) of the approximation, as well as the mass (m) of our particle and Planck's constant (h), all in SI units.

The wave function solutions ψ of our discretised system are finite sets containing approximations of $\psi(x)$ over the finite number of coordinate points. We can therefore describe the wave functions of the discretised system as vectors $(\psi(0), \psi(l), \psi(2l), ..., \psi(Nl))$, with N the resolution of our system and $Nl = L$ defining l. Discretising the wave function in Schrödinger's equation (3) allows us to approximate the non-relativistic Hamiltonian,

$$\hat{H} = \left[\frac{-\hbar^2}{2m}\nabla^2 + U(\vec{r})\right],$$

as a matrix operating on the wave function vector. The eigenfunction problem of equation (3) therefore becomes a matrix eigenvector problem when we discretise the system. In this way, we create a model for our system that is open to numerical methods.

The next task is then to construct the matrices that will be used to approximate the Hamiltonian of our system. The Hamiltonian has two terms, corresponding to the kinetic and potential energies, respectively. We will here first discuss how to discretise the kinetic term.

As kinetic energy necessarily has to do with motion, we have to construct a matrix equivalent of a derivative. In particular, the Laplacian ∇^2 in one dimension is the second derivative along that dimension, so that our goal is to model a second derivative.

For a given wave function $\psi(x)$ the x-derivative at a given point x' is approximated by $(\psi(x' + l) - \psi(x' - l))/2l$. The matrix that approximates the x-derivative operator is then given by a square $N \cdot N$ matrix, so that when it is applied to the vector $\vec{\psi}$ containing N

data points of the wave function ψ over the interval of the box, it returns a vector with N elements containing the values of the x-derivative over the interval. This operator is a sparse banded matrix with elements $(2l)^{-1}$ on the first upper off-diagonal, and elements $-(2l)^{-1}$ on the first lower off-diagonal. A sparse matrix is a matrix in which most elements are zero. Periodic boundary conditions can be imposed by taking the elements at $(1, N)$ and $(N, 1)$ to be $-(2l)^{-1}$ and $(2l)^{-1}$ respectively. The whole situation is shown schematically by

$$\frac{1}{2l}\begin{pmatrix} 0 & 1 & 0 & 0 & \cdots \\ -1 & 0 & 1 & 0 & \cdots \\ 0 & -1 & 0 & 1 & \cdots \\ 0 & 0 & -1 & 0 & \cdots \\ \vdots & \vdots & \vdots & \vdots & \ddots \end{pmatrix}\begin{pmatrix} \psi(0) \\ \psi(l) \\ \psi(2l) \\ \psi(3l) \\ \vdots \end{pmatrix} = \frac{1}{2l}\begin{pmatrix} \psi(l) - \psi(L) \\ \psi(2l) - \psi(0) \\ \psi(3l) - \psi(l) \\ \psi(4l) - \psi(2l) \\ \vdots \end{pmatrix}.$$

For the second x-derivative of $\psi(x)$ at x', we use $(\psi(x'+2l) - 2\psi(x') + \psi(x'-2l))/4l^2$. The second derivative matrix can therefore be constructed by simply taking the matrix product of the first derivative matrix with itself. In this way, the one-dimensional Laplacian ∇^2 is approximated by the matrix

$$\frac{1}{4l^2}\begin{pmatrix} -2 & 0 & 1 & 0 & \cdots \\ 0 & -2 & 0 & 1 & \cdots \\ 1 & 0 & -2 & 0 & \cdots \\ 0 & 1 & 0 & -2 & \cdots \\ \vdots & \vdots & \vdots & \vdots & \ddots \end{pmatrix}.$$

By multiplying the resulting sparse $N \cdot N$ matrix with $-\hbar^2/2m$, we obtain the kinetic term of the Hamiltonian.

Any potential $U(x)$ that could be added to the Hamiltonian would take the form of a sparse diagonal $N \cdot N$ matrix with elements $U(x)$ along the diagonal, so that the potential operates on the wave function, as shown here,

$$\begin{pmatrix} U(0) & 0 & 0 & 0 & \cdots \\ 0 & U(l) & 0 & 0 & \cdots \\ 0 & 0 & U(2l) & 0 & \cdots \\ 0 & 0 & 0 & U(3l) & \cdots \\ \vdots & \vdots & \vdots & \vdots & \ddots \end{pmatrix}\begin{pmatrix} \psi(0) \\ \psi(l) \\ \psi(2l) \\ \psi(3l) \\ \vdots \end{pmatrix} = \begin{pmatrix} U(0) * \psi(0) \\ U(l) * \psi(l) \\ U(2l) * \psi(2l) \\ U(3l) * \psi(3l) \\ \vdots \end{pmatrix}.$$

In this way, the zero boundary condition of $\psi(0) = \psi(L) = 0$ can be set by adding a sparse potential matrix with large positive elements at $(1, 1)$ and (N, N).

Once the Hamiltonian sparse matrix has been defined, the *eighs* function from scipy can be applied to obtain the numerical eigenvalues and eigenvectors of the Hamiltonian, which correspond to our wave functions and energies, respectively. As input, this function requires a real symmetric square matrix or complex Hermitian matrix and an integer specifying the number of requested eigenvalues and eigenvectors, as well as a method to determine which solutions are constructed.

There are two possible parameters that can be used to specify the desired method of solving the eigenvalue problem. The first of these is based on using the *which* parameter,

which can for example take in the argument *'LM'* to make the *eighs* function return only the largest magnitude eigenvalues and their corresponding eigenvectors. As we are primarily interested in the first few smallest eigenvalues, the *which* parameter would have to take the value $'SA'$ or $'SM'$, corresponding to the smallest algebraic and the smallest magnitude solution, respectively. Though this is the most straightforward method, it is inadvisable due to the nature of the *eighs* function ([18], pp. 22-29, pp. 60-62)([30], pp. 121-125, pp. 141-144).

The *eighs* function is based on the implicitly restarted Lanczos method, which excels at constructing the $m << N$ maximum eigenvalues and their corresponding eigenvectors for very large sparse matrices. It, however, quickly breaks down when directly used to find the minimum eigenvalues of such a matrix. In order to work around this problem, another parameter is available to the *eighs* function, which makes use of the following simple trick. A reader with little interest as to the mathematics of the method may wish to skip the next two paragraphs ([18], pp. 22-29, pp. 60-62)([30], pp. 121-125, pp. 141-144).

For the simplest case, let $\vec{v}$ be an eigenvector of the square matrix A, with corresponding eigenvalue λ, so that

$$A\vec{v} = \lambda\vec{v}. \tag{4}$$

Since equation (4) has non-zero solutions if and only if the determinant of A is non-zero, we will assume A has an inverse. Multiplying (4) to the left with A^{-1} gives

$$A^{-1}\vec{v} = \frac{1}{\lambda}\vec{v}. \tag{5}$$

Therefore, the eigenvectors of A are also eigenvectors of A^{-1}, but the eigenvectors that have maximal eigenvalues as eigenvectors of A^{-1} have minimal eigenvalues as eigenvectors of A. We can therefore optimize the implicitly restarted Lanczos method for finding the minimum eigenvalues and their corresponding eigenvectors by constructing the maximal eigenvalues of the inverse matrix and inverting the eigenvalues, while keeping the eigenvectors ([18], pp. 22-29, pp. 60-62)([30], pp. 121-125, pp. 141-144).

The implicitly restarted Lanczos method operates on the generalized eigenvalue problem. Here, we will show that under the right circumstances, this generalized problem reduces to the problem we want to investigate. In the generalized eigenvalue problem, we have

$$A\vec{v} = \lambda M\vec{v}. \tag{6}$$

Substracting $\sigma M\vec{v}$ from both sides of equation (6) gives

$$(A - \sigma M)\vec{v} = (\lambda - \sigma)M\vec{v}, \tag{7}$$

which can be written as

$$(A - \sigma M)^{-1}M\vec{v} = \mu\vec{v}, \tag{8}$$

where μ is defined as

$$\mu = \frac{1}{\lambda - \sigma}. \tag{9}$$

This spectral transformation transforms eigenvalues λ to eigenvalues $\mu = 1/(\lambda - \sigma)$, so that the eigenvalues λ that are close to σ correspond to the maximum eigenvalues of the eigenvalue

problem of equation (8). In other words, using the spectral transformation of equation (9), the convergence of the implicitly restarted Lanczos algorithm is enhanced for eigenvalues λ close to σ. Taking $\sigma = 0$ reduces the problem to the simple inverted eigenvalue problem that we are interested in ([18], pp. 22-29, pp. 60-62)([30], pp. 121-125, pp. 141-144).

The *eighs* function has a parameter σ so that if we set it to $\sigma = 0$, the *eighs* function solves the inverted eigenvalue problem and then inverts the solutions. This results in greatly improved accuracy and computation time when compared to the $which =' SA'$ method, and is therefore greatly preferable ([18], pp. 22-29, pp. 60-62)([30], pp. 121-125, pp. 141-144).

Though very fast and accurate, the implicitly restarted Lanczos method of ARPACK has some undesirable properties. In particular, the method gives rise to an unwanted two-fold degeneracy of the eigenvalues. Moreover, the resulting eigenvectors themselves contain two solutions with the same shape but with different amplitudes. In many respects, this dual solution form of the eigenvectors leaves the results intact, and can often be ignored. In particular, the numerical eigenvalues are calculated correctly, but the wave functions have to be normalized afterwards. In the context of visualization, it may however be preferable to strip the eigenvector solutions of the small amplitude wave solution. This is discussed in section 3.5.

The topic of finding a better algorithm, which can compete with implicitly restarted Lanczos algorithm and does not suffer from this unwanted degeneracy forming, will not be investigated further here. Re-orthogonalization techniques seem promising, but may take a toll on computation time. Research has been done on this topic [16] [23] [27] [30].

Now that we have the numerical solutions of our wave functions ψ and their corresponding energies, we can find the probability densities $|\psi|^2$ by multiplying ψ with its complex conjugate ψ^*. We can then plot the probability densities against the position coordinates in the box, connecting the finite number of data points by lines. For this we use matplotlib's *plot* function. In this way, if the resolution is chosen sufficiently large, the numerical solutions quickly approach the analytical solutions, as we will show in section 4.1.

3.3 Modelling of two-dimensional systems

Now that we know how to solve the non-relativistic time-independent Schrödinger equation (3) in one dimension for several potentials, we can expand our horizons to two dimensions. In particular, we will here describe a method to numerically solve the non-relativistic, time-independent, Schrödinger equation in two dimensions for a single electron in a box under the influence of an arbitrary potential $U(x, y)$. For the most part this box is assumed to be rectangular.

The method for constructing such a two-dimensional simulation follows the same essential steps as the one-dimensional case. First, we define a set of parameters that specify our system, in this case a two-dimensional box containing a single electron. The dimensions and resolutions in the x- and the y-directions are denoted respectively by L_x and L_y, and N_x and N_y.

The vector describing our two-dimensional wave function ψ is of a somewhat different form than in the one-dimensional case. In the two-dimensional case, the first N_x elements of our vector describe the wave function over the entire x-interval with $y = 0$. Subsequently the second N_x elements describe the wave function, again over the entire x-interval, but now for

$y = l_y$ with $l_y N_y = L_y$. Another way to understand this format is to see the wave function vector for a two-dimensional system as the combination of N_y wave function vectors for one-dimensional systems with resolution N_x, so that the union of these one-dimensional systems equals our two-dimensional system.

Because we can understand our two-dimensional system as the union of N_y one-dimensional systems, we can divide the problem at hand into two sub-problems. First, we need a method to solve the one-dimensional problems. Such a method is described in the section on one-dimensional modelling. The second sub-problem is then to combine these one-dimensional solutions into a solution for the two-dimensional problem.

In order to solve both sub-problems elegantly in one move we define two one-dimensional derivative matrices, one with dimensions $N_x \cdot N_x$ and the other with dimensions $N_y \cdot N_y$. These will be called D_x and D_y, respectively. They are defined using the exact same method as for the one-dimensional simulations. With these two first-derivative matrices, we construct the one-dimensional second-derivative matrices $D_x^2 = D_x \cdot D_x$ and $D_y^2 = D_y \cdot D_y$. We call these derivative matrices one-dimensional, in the sense that they define derivatives on one-dimensional systems of resolution N_x and N_y, respectively.

As an aside, if the resolutions in the x- and y-directions are set equal, we can choose to add a potential $U(x, y)$ to $-(\hbar^2/2m)D_x^2$ now, in which case $U(x, y)$ will be symmetrical under rotation from positive x- to y-axis and vice versa, so that $U(x = a, y = b) = U(x = b, y = a)$. For simple, symmetric potentials such as a central square barrier, this method offers an easy way of adding a potential. If, instead, we want a potential that does not exhibit such a symmetry, or if our system has different resolutions in the x- and y-directions, we should add a potential not to the one-dimensional kinetic energy operator, but rather to the two-dimensional kinetic energy operator defined in the next paragraph.

We have defined second-derivative matrices in the x- and the y-directions, so now, to solve the second sub-problem, we must combine these in such a way that our results apply to the two-dimensional system. The most elegant method for this task is based on the Kronecker product ($\otimes$), which is supported by the *scipy.sparse.kron* function.

In order to take the partial second derivative in the x-direction, we take the Kronecker product $I_y \otimes D_x^2$ of the identity matrix I_y, with dimensions $N_y \cdot N_y$, with the regular second derivative D_x^2 in the x-direction. This is shown schematically by

$$\left[I_y \otimes D_x^2\right] \vec{\psi}(x, y) = \begin{pmatrix} D_x^2 & 0 & 0 & 0 & \cdots \\ 0 & D_x^2 & 0 & 0 & \cdots \\ 0 & 0 & D_x^2 & 0 & \cdots \\ 0 & 0 & 0 & D_x^2 & \cdots \\ \vdots & \vdots & \vdots & \vdots & \ddots \end{pmatrix} \begin{pmatrix} \psi(0,0) \\ \psi(l_x,0) \\ \vdots \\ \psi(L_x,0) \\ \psi(0,l_y) \\ \psi(l_x,l_y) \\ \vdots \end{pmatrix} = \begin{pmatrix} \frac{\partial^2}{\partial x^2}\psi(0,0) \\ \frac{\partial^2}{\partial x^2}\psi(l_x,0) \\ \vdots \\ \frac{\partial^2}{\partial x^2}\psi(L_x,0) \\ \frac{\partial^2}{\partial x^2}\psi(0,l_y) \\ \frac{\partial^2}{\partial x^2}\psi(l_x,l_y) \\ \vdots \end{pmatrix}.$$

The zeros in the $I_y \otimes D_x^2$ matrix represent $N_x \cdot N_x$ null-matrices.

Similarly, though perhaps less intuitively, the second partial derivative in the y-direction

is given by $D_y^2 \otimes I_x$, where I_x is the identity matrix with dimensions $N_x \cdot N_x$, as shown here

$$\left[D_y^2 \otimes I_x\right] \vec{\psi}(x,y) = \frac{1}{4l_y^2} \begin{pmatrix} -2I_x & 0 & I_x & 0 & \cdots \\ 0 & -2I_x & 0 & I_x & \cdots \\ I_x & 0 & -2I_x & 0 & \cdots \\ 0 & I_x & 0 & -2I_x & \cdots \\ \vdots & \vdots & \vdots & \vdots & \ddots \end{pmatrix} \begin{pmatrix} \psi(0,0) \\ \psi(l_x,0) \\ \vdots \\ \psi(L_x,0) \\ \psi(0,l_y) \\ \psi(l_x,l_y) \\ \vdots \end{pmatrix} = \begin{pmatrix} \frac{\partial^2}{\partial y^2}\psi(0,0) \\ \frac{\partial^2}{\partial y^2}\psi(l_x,0) \\ \vdots \\ \frac{\partial^2}{\partial y^2}\psi(L_x,0) \\ \frac{\partial^2}{\partial y^2}\psi(0,l_y) \\ \frac{\partial^2}{\partial y^2}\psi(l_x,l_y) \\ \vdots \end{pmatrix}.$$

Now, we are able to construct ∇^2 in two dimensions by using

$$\nabla^2 = \nabla_x^2 + \nabla_y^2 = I_y \otimes D_x^2 + D_y^2 \otimes I_x. \tag{10}$$

The two-dimensional second-derivative operator is therefore approximated by a sparse square matrix with dimension $N_x N_y \cdot N_x N_y$.

We can now construct the two-dimensional Hamiltonian matrix by simply multiplying ∇^2 by $-\hbar^2/2m$ and, if no potential was added before, adding a potential now. A potential matrix $U(x,y)$ takes the form of an $N_x N_y \cdot N_x N_y$ diagonal matrix with the design

$$\begin{pmatrix} U(0,0) & 0 & \cdots & \cdots & \cdots & \cdots \\ 0 & U(l_x,0) & \cdots & \cdots & \cdots & \cdots \\ \vdots & \vdots & \ddots & \cdots & \cdots & \cdots \\ \vdots & \vdots & \vdots & U(L_x,0) & 0 & \cdots \\ \vdots & \vdots & \vdots & 0 & U(0,l_y) & \cdots \\ \vdots & \vdots & \vdots & \vdots & \vdots & \ddots \end{pmatrix}.$$

To impose the boundary condition of a rectangular box of dimensions $L_x \cdot L_y$, all elements $U(0,y) = U(L_x,y) = U(x,0) = U(x,L_y)$ are set to some large positive constant. A square box can thus be imposed by taking $L_x = L_y$. In order to implement periodic boundary conditions, at the beginning one simply constructs the one-dimensional derivative matrices D_x and D_y and then includes periodicity by adding $-(2l_x)^{-1}$ and $(2l_x)^{-1}$ at $(1,N_x)$ and $(N_x,1)$ and $-(2l_y)^{-1}$ and $(2l_y)^{-1}$ at $(1,N_y)$ and $(N_y,1)$ to D_x and D_y, respectively. This periodicity is then automatically carried along to the two-dimensional Hamiltonian.

The eigenvectors of the resulting Hamiltonian matrix are one-dimensional arrays of length $N_x N_y$, so that the first N_x elements represent $\psi(x, y = 0)$, and the second N_x elements $\psi(x, y = l_y)$, and so forth. Notice also that we cannot choose N_x and N_y very large, as computation time increases quadratically.

We can now find the smallest eigenvalues (and their corresponding eigenvectors) of the Hamiltonian matrix of the two-dimensional system. Notice that we can safely use the *eighs* function for this once again, because the identity matrix is symmetrical, and the sum and Kronecker product of two symmetrical matrices is itself symmetrical. By applying the *eighs* function with parameter $\sigma = 0$ to the Hamiltonian matrix described above, we construct

the smallest eigenvalues and the corresponding eigenvectors for the two-dimensional system. These represent numerical approximations of the desired energy and wave function solutions of our two-dimensional system, respectively.

Plotting the resulting probability density of the eigenfunctions in its current format unto two dimensions using matplotlib results in a potentially complicated plot, where the probability densities over the entire x-interval for subsequent y-coordinates are plotted next to each other. This is generally discouraged, as such plots often confuse rather than elucidate. Instead, three-dimensional plots or two-dimensional density plots are preferred.

In order to plot the resulting probability density in three dimensions, we rework the one-dimensional array containing the probability density corresponding to a given wave function solution into a two-dimensional array, so that the first N_x elements of the one-dimensional array form the first row of the two-dimensional array, the second N_x elements the second row, until we have a two dimensional array with N_y rows and N_x columns. We can now plot this two-dimensional array against the two-dimensional mesh of x- and y-coordinates, constructed using numpy's *meshgrid* function. For this, we use matplotlib's *mpl_toolkits.mplot3d.Axes3D* function.

3.4 Lorentzian Broadening and the Local Density of States

The STM patterned indium arsenide artificial lattice, though less than molecular graphene, shows a broadening of the local density of states, due to scattering to the bulk, as discussed in section 2.1. This broadening can, phenomenologically, be modeled by a Lorentzian function. The probability density of such a function is given by

$$f(x) = \frac{\gamma}{\gamma^2 + (x - x_0)^2}. \tag{11}$$

Here, γ is the scale parameter that determines the width of the function. A plot of a Lorentzian function is given in figure 9, which indeed shows a peak with an amount of broadening.

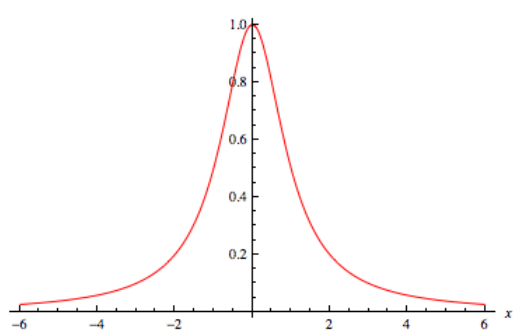

Figure 9: Plot of a Lorentzian function.

Using these Lorentzian functions, broadening due to scattering can be built into the numerical model ([10], p. 307)([13], p. 132)([15], pp. 527-528)([20], p. 2)([28], p. 677).

The local density of states, without any broadening, is given by

$$LDOS(E, \vec{x}) = \sum_{E'} |\psi_{E'}(\vec{x})|^2 \delta(E - E'). \tag{12}$$

The lack of broadening is evident from the presence of the delta function, which ensures that the local density of states is only non-zero at the eigenenergies E' of the system. In order to include a broadening, the delta function in equation (12) is replaced by a Lorentzian function,

$$LDOS(E, \vec{x}) = \sum_{E'} |\psi_{E'}(\vec{x})|^2 \frac{\gamma}{\gamma^2 + (E - E')^2}. \tag{13}$$

The code above constructs numerical solutions for the wave functions and the corresponding eigenenergies, and equation (13) shows that, when a parameter γ is supplied, the local density of states can be constructed from these by a simple summation.

3.5 Stripping functions

Because of the way the numerical eigenvectors are constructed using the implicitly restarted Lanzcos algorithm, each eigenvector in fact contains two solutions, so that the elements of one solution are all on the even indices of the vector, while the elements at the odd indices form the second solution. The two solutions are of the same form, but have different amplitude. We will call the solution with the smaller amplitude the small amplitude wave solution. The repeated jumping between large and small amplitude wave solution makes the plots look 'filled in', as shown in figure 10.

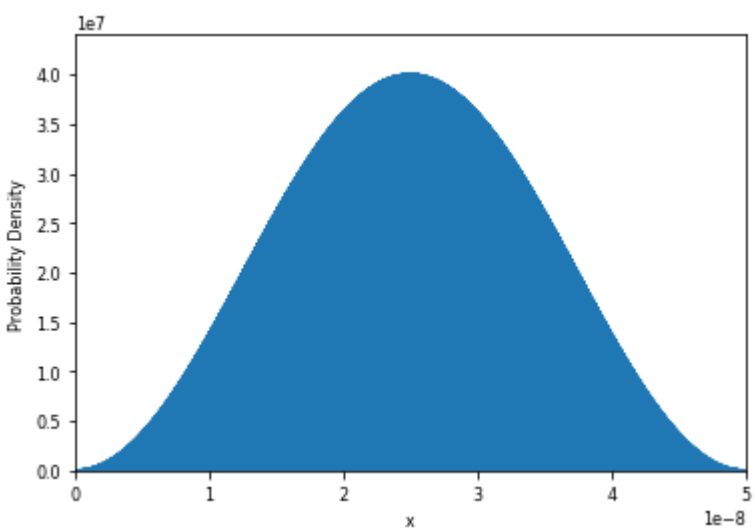

Figure 10: Unstripped plot of a numerical solution for a particle in a one-dimensional box.

As the two solutions are of the same form, we only need one of the two, because, when it is properly normalized, either solution contains all the physical content. Therefore, mostly for aesthetic reasons, it can be considered to either strip the constructed eigenvector of one

of the two solutions, or to sum eigenvectors in such a way that one of the two solutions effectively vanishes. If a solution is stripped away here, it is arbitrarily chosen to always be the small amplitude wave solution.

For the three-dimensional plots, it can also be advantageous in terms of computation time to strip the constructed eigenvectors of the small amplitude solution, as it halves the number of data that is to be plotted, without losing any essential visual information. It should, however, be noted that the majority of the computation time comes from modeling systems, and not from plotting their solutions. It is therefore advisable to plot the solutions of two-dimensional systems as density plots, as these require little computation time to begin with. However, if three-dimensional plots are preferred, and a large number of plots has to be made, the stripping functions are a good option.

For a one-dimensional simulation, it is straightforward to write a function that accepts an array of a probability density that contains a small amplitude wave solution as input and returns an array containing only the large amplitude wave solution probability density. Note that the elements of the constructed eigenvectors iterate between the large and the small wave solutions. Such a stripping function constructs an array containing each element of the old array that satisfies the property that the element minus its successor is positive. If this method runs well, we expect to construct an array with approximately half the elements of the old array. This is indeed the case, and the method works well. A plot of a numerical solution stripped in this way is shown in figure 11.

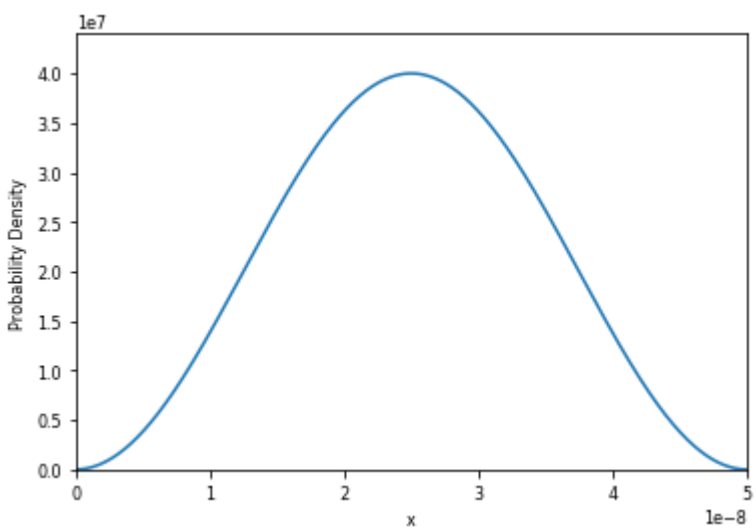

Figure 11: Stripped plot of a numerical solution for a particle in a one-dimensional box.

For two-dimensional simulations, it becomes a more complicated task to strip the small amplitude wave solution. We first construct a one-dimensional array, itself containing one-dimensional arrays encompassing the probability density of a given wave function solution over the entire x-interval for a given y-coordinate. This is done in the same way as for the regular three-dimensional plot. Then, we recursively apply the previous one-dimensional stripping function to each of the elements of this array of arrays, so that we obtain a new array of arrays, of which each element is approximately halved in length. In order to rework

this array into an ordered two-dimensional array with a set amount of columns, each of its elements is edited to have exactly half the number of elements as the resolution in the x-direction. If an array is too short, zeros are appended to the left and the right until it has the desired length. If an array is too long, elements are stripped off at the left and the right until it reaches the desired length. In this way, we construct a two-dimensional array with N_y rows and $N_x/2$ columns. We can now plot this two-dimensional array against the two-dimensional mesh of the y-coordinates and half of the x-coordinates. For this, we again use matplotlib's $mpl\_toolkits.mplot3d.Axes3D$ function. For sufficiently large resolutions, the above function yields excellent plots of the probability densities in three dimensions, with much less computation time than the full plot. A plot of a numerical solution, stripped in this way, is given in figure 12.

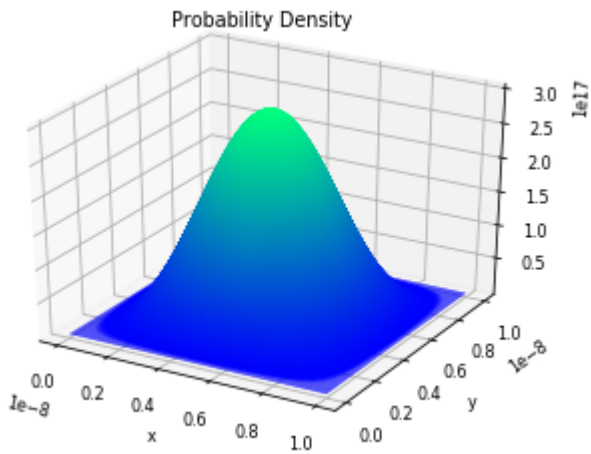

Figure 12: Stripped plot of a numerical solution for a particle in a two-dimensional box.

Alternatively, the constructed eigenvectors that are degenerate due to the Lanczos algorithm can be summed in order to effectively filter out the small amplitude wave solution. Though not fully understood, it seems to be the case that, if the small amplitude wave solution resides on the even indices in one solution, it resides on the odd indices of its degenerate solution. Since the small amplitude wave solution is generally much smaller than the large amplitude one, adding the two degenerate solutions effectively eliminates the small amplitude wave solution, except for a small vertical broadening, often observed at the peaks of the solutions. A plot of a numerical solution, filtered in this way, is given in figure 13

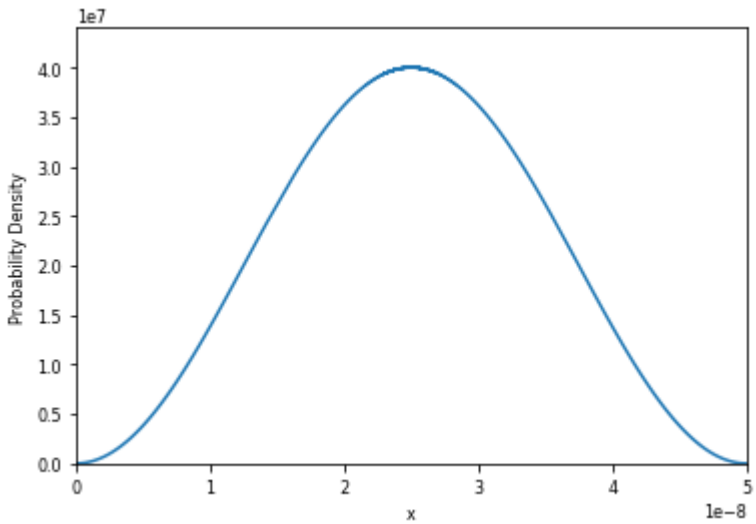

Figure 13: Filtered plot of a numerical solution for a particle in a one-dimensional box.

4 Results

In order to test whether the code outlined in section 3 functions well in general, as well as for the particular systems that are of interest in this work, we first supply and discuss the obtained solutions for several more elementary systems with analytical solutions. First, we will look at the solutions for one-dimensional systems, after which we will turn to two-dimensional systems. After verifying that the code indeed works well for these more elementary systems, and in particular that it works well for the non-central barrier/well potential, which will be the building block for all subsequent systems, we will treat the linear indium arsenide chain in one and two dimensions, and compare our theoretical results with the empirical results from Pham et al. [24]. Finally, we will supply and discuss the results obtained for a variation of the hexagonal quantum ring, and again compare these with the empirical results for the same system from Pham et al. [24].

4.1 One-dimensional simulations

For the following plots we modelled an electron of mass 9.109×10^{-31} kg in a one-dimensional box of length 1×10^{-7} m with resolution $N = 1001$. With all parameters in SI units, we take the reduced Planck constant as $\hbar = 1.055 \times 10^{-34}$ Js.

Figure 14 is a plot of the probability distribution for the first solution of an electron in the previously described one-dimensional box, with a zero potential $U(x) = 0$ over the interval of the box. The blue line shows the analytical solution for this system, and the green dotted line shows the numerical solution constructed using the code described in section 3.2. Notice that we stripped the numerical low-amplitude wave solution using the stripping function as described in section 3.5. The plotted numerical solution matches the analytical one very well. This means that our code successfully models the wave functions and probability densities for simple systems such as a particle in a box.

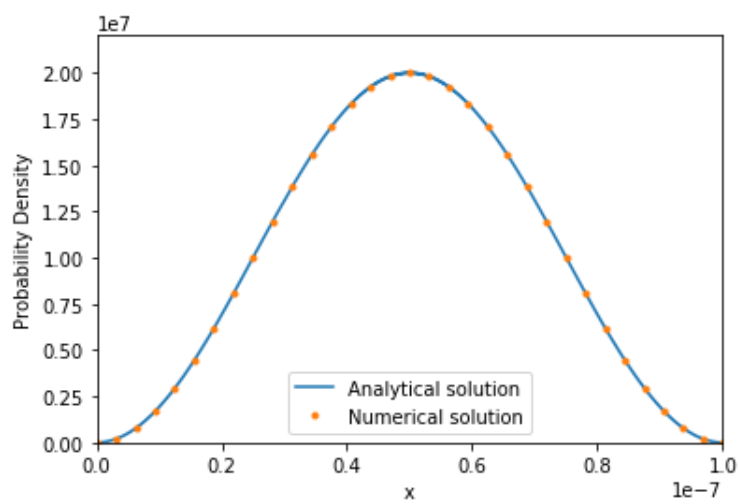

Figure 14: Stripped plot of the numerical solution of $|\psi_1(x)|^2$ for a particle in a 1D box, shown by the orange dots, together with the analytical solution for the same wave function, shown by the blue line.

For further simulations it is, however, also necessary that we successfully describe the behaviour of more complicated systems. Moreover, our models should return good approximations of the energies corresponding to each wave function. We will, therefore, first examine the numerical solutions for a more complicated potential, after which we will take a closer look at the computed numerical energy values.

Figure 15 is a plot of the analytic and numerical solutions of the probability distribution for the thirteenth solution of an electron in the one-dimensional box, under the influence of a harmonic potential $U_{har}(x) = \frac{1}{2}k(x - L_x/2)$. Here, the length of the box is $L_x = 1 \times 10^{-7}$m and the force constant is $k = 1 \times 10^{-5}$kg/s^2. Notice that we stripped the numerical low-amplitude wave solution. Again, the plot of our numerical simulation matches the expected analytical solution very well.

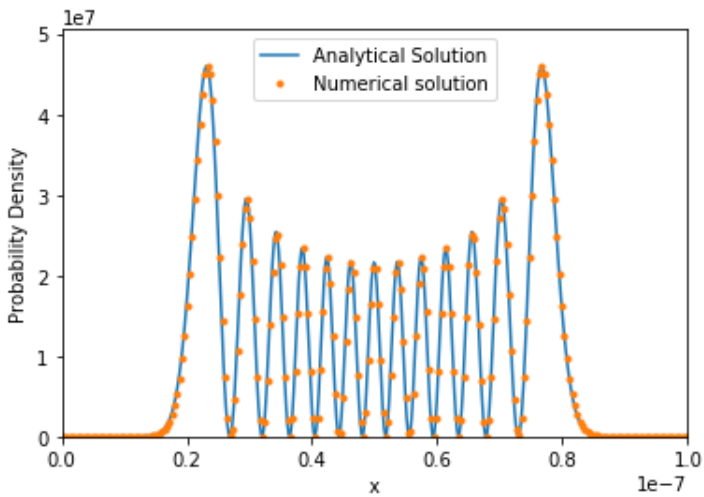

Figure 15: Stripped plot of the numerical solution of $|\psi_{12}(x)|^2$ for a particle in a 1D box with a harmonic potential, shown together with the analytical solution for the same wave function.

Of particular interest are the numerical solutions for systems with non-central barrier or well potentials. By summing a number of such potentials, we will be able to construct the muffin-tin potentials which will be used to model the indium arsenide systems studied here. The muffin-tin approximation method has been successfully used in the modeling of a number of artificial lattice systems [7] [8] [13] [14] [28] [29].

An example of a numerical solution for a non-central barrier potential, constructed using the code described in section 3.2, is given in figure 16. In particular, figure 16 is a stripped plot of the numerical solution of the probability density for the first solution of an electron in the one-dimensional box described above, under the additional influence of a non-central barrier potential of width 5×10^{-9}m and magnitude 1×10^{-19}J, centered around $x = 3.5 \times 10^{-8}$m. The plot matches the expected result of a particle in a modified, shortened, box.

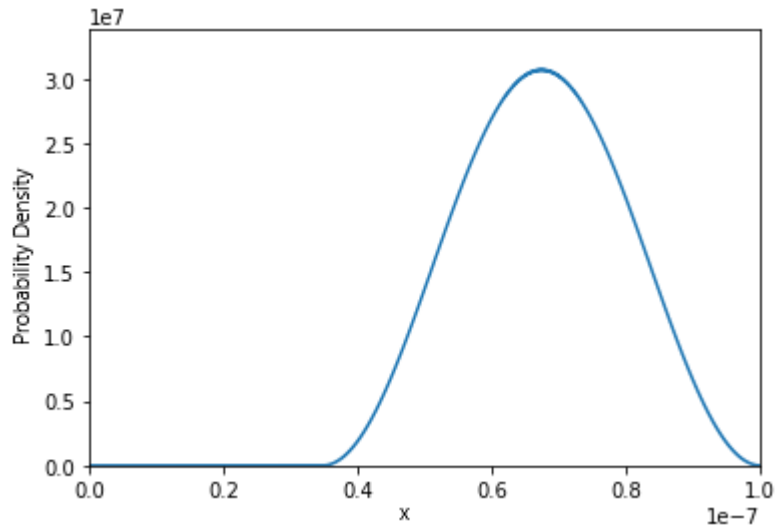

Figure 16: Filtered plot of the numerical solution of $|\psi_1(x)|^2$ for a particle in a 1D box with a non-central barrier potential of width 5×10^{-9}m and magnitude 1×10^{-19}J, centered around $x = 3.5 \times 10^{-8}$m.

Besides the numerically constructed wave functions, the numerical energies for one-dimensional systems, too, are modelled well by the code. This can be seen by comparing the numerically constructed energies to the well known analytic energy solutions for the particle in a one-dimensional box, as well as those for a particle in a one-dimensional harmonic potential.

Two tables with energies are supplied in table 1. Table 1a contains numerical and analytical solutions for the lowest five energy states of an electron in the previously described one-dimensional box. Table 1b contains such energies in the case of the same harmonic potential as described before. Notice that the numerical and analytical energy solutions match very well for both potentials.

Particle in a Box	
Numerical E_n	Analytical E_n
$3.7635 \times 10^{-5} eV$	$3.7635 \times 10^{-5} eV$
$1.5054 \times 10^{-4} eV$	$1.5054 \times 10^{-4} eV$
$3.3871 \times 10^{-4} eV$	$3.3872 \times 10^{-4} eV$
$6.0213 \times 10^{-4} eV$	$6.0216 \times 10^{-4} eV$
$9.4080 \times 10^{-4} eV$	$9.4088 \times 10^{-4} eV$

Harmonic Potential	
Numerical E_n	Analytical E_n
$1.0919 \times 10^{-3} eV$	$1.0908 \times 10^{-3} eV$
$3.2755 \times 10^{-3} eV$	$3.2727 \times 10^{-3} eV$
$5.4588 \times 10^{-3} eV$	$5.4545 \times 10^{-3} eV$
$7.6415 \times 10^{-3} eV$	$7.6362 \times 10^{-3} eV$
$9.8241 \times 10^{-3} eV$	$9.8180 \times 10^{-3} eV$

Table 1: Comparison between numerical and analytical energies for one-dimensional systems.

The computer program for one-dimensional simulations runs fast and constructs solutions that match excellently with analytical predictions for a number of simple and more complicated potentials. In particular, since it runs well for systems with non-central barrier and well potentials, it can be expected to run well for one-dimensional muffin-tin simulations, since the muffin-tin potential will be constructed using a sum of such non-central potentials.

4.2 Two-dimensional Simulations

In order to test our code for simulations of two-dimensional systems, we again plot our numerical solutions for a number of different potentials, and compare the numerically constructed energies of several systems with the well-known energy solution for those systems. In this section, every plotted solution is unstripped.

For the following plots, we modelled an electron of mass 9.109×10^{-31}kg in a two-dimensional square box of dimensions $(1 \times 10^{-8}) \times (1 \times 10^{-8})\text{m}^2$ with resolutions in the x- and y-direction $N_x = N_y = 301$. Again we take $\hbar = 1.055 \times 10^{-34}$Js. Figure 17 shows both three-dimensional and density plots of the numerical solutions for a number of example potentials, as well as density plots for the corresponding analytical solutions. The colour scale for the three-dimensional plots, supplied in figure 17, applies to all three-dimensional plots in this work, while the colour scale of the density plot, shown in the same figure, applies both to all contour and density plots.

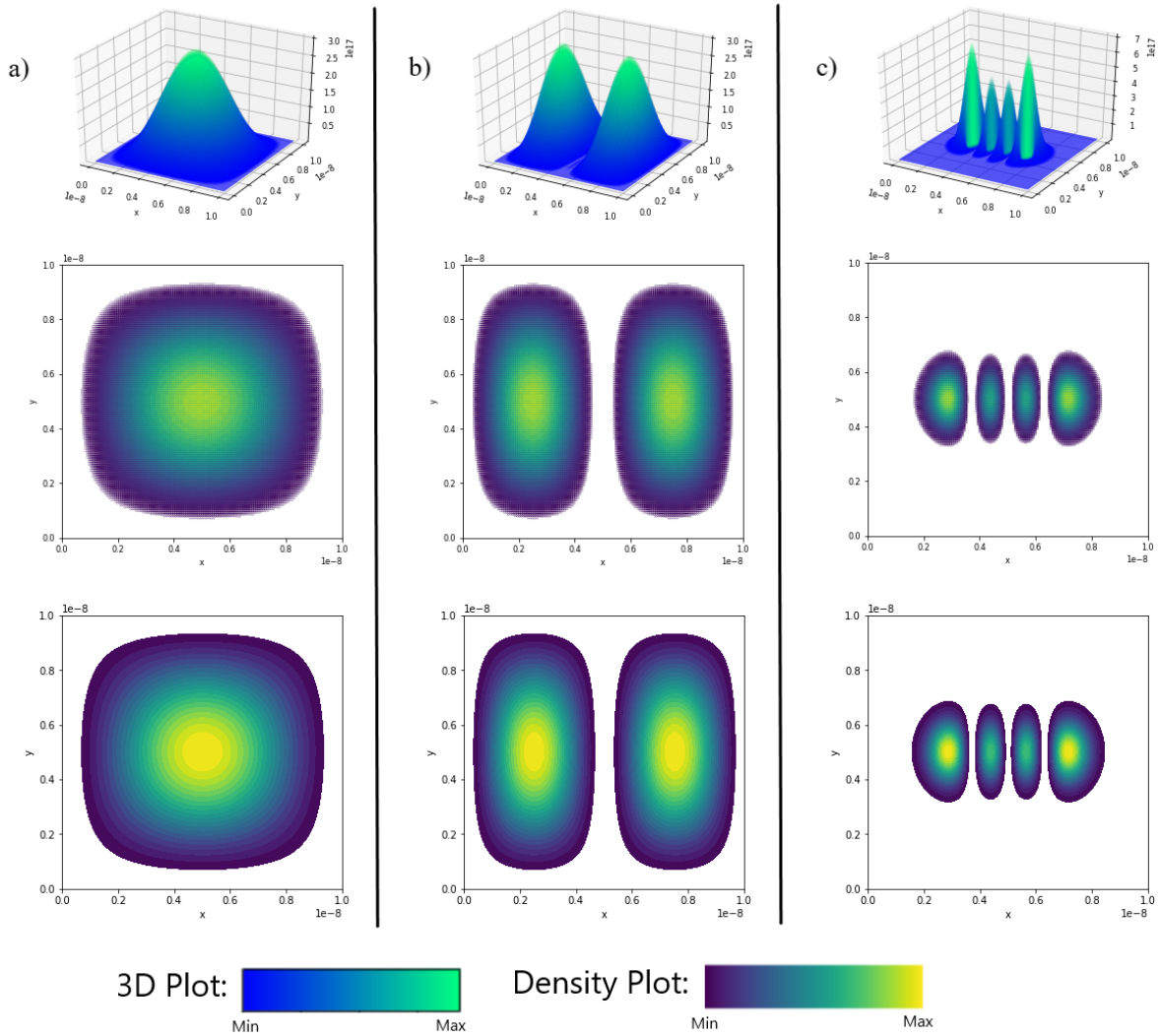

Figure 17: **a)** The top figure shows a three-dimensional plot of the numerical ground state solution for an electron in the previously described two-dimensional box, while the middle figure shows a density plot of the same solution. The bottom figure is a density plot of the analytical solution of the same system.
b) The top figure shows a three-dimensional plot of the numerical second overtone solution for an electron in the previously described two-dimensional box, while the middle figure shows a density plot of the same solution. The bottom figure is a density plot of the analytical solution of the same system.
c) The top figure shows a three-dimensional plot of the numerical third overtone solution for an electron in the previously described two-dimensional harmonic potential, while the middle figure shows a density plot of the same solution. The bottom figure is a density plot of the analytical solution of the same system.

In figure 17a we show a three-dimensional plot and a density plot of the numerically constructed probability distribution for the first solution of an electron in the previously

described two-dimensional box, together with a density plot of the analytical solution of the same system. Notice we did not strip the solution of the low amplitude wave solution, since time was not a constraint. The density plot of the numerical solution strongly matches the plot of the analytical solution.

In figure 17b we plot both the numerical and analytical solutions of the second solution of an electron in the previously described two-dimensional box. The figures show that the numerical simulations accurately predict the behaviour of higher-order solutions for a particle in a box.

In figure 17c the fourth solution of an electron in the square box under the influence of a harmonic potential $U(x,y) = \frac{1}{2}k(\left|x - \frac{L_x}{2}\right| + \left|y - \frac{L_y}{2}\right|)^2$ is depicted, where L_x and L_y are the x- and y-dimensions of the two-dimensional box and $k = 2 \times 10^{-2}\text{kg/s}^2$ is the force constant. We see the numerical simulations predict the behaviour of the well known harmonic oscillator well.

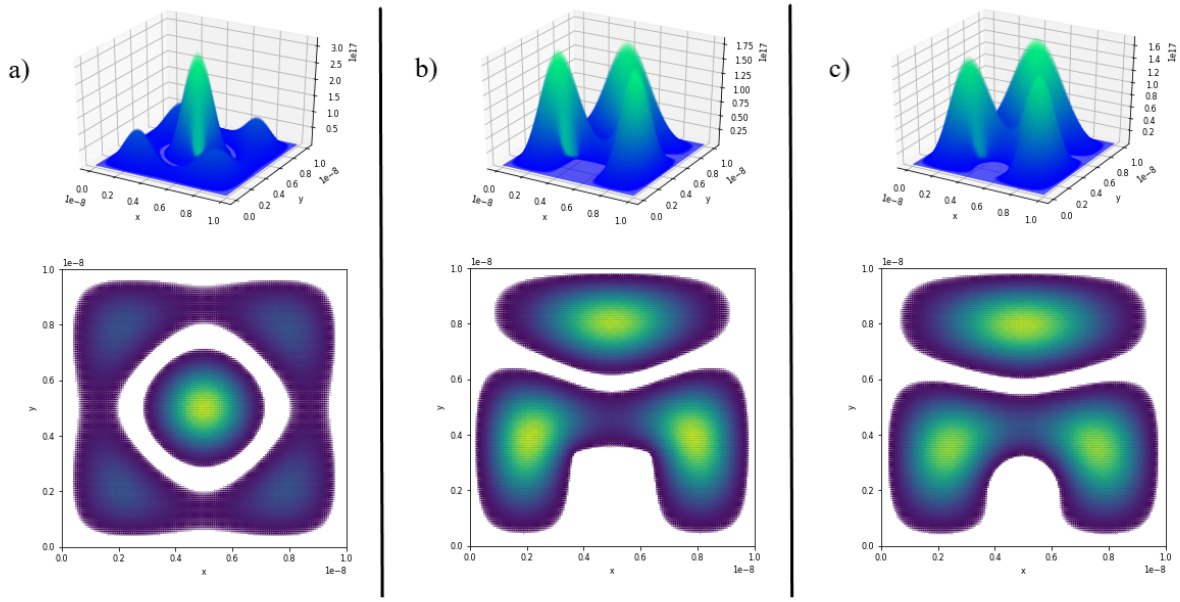

Figure 18: **a)** The top figure shows a three-dimensional plot of the numerical solution of the fourth overtone for an electron in the square box under the influence of a central square well potential, and the bottom figure shows a density plot of the same solution.
b) The top figure shows a three-dimensional plot of the numerical third overtone solution for an electron in the square box under the influence of a non-central square barrier potential, and the bottom figure shows a density plot of the same solution.
c) The top figure shows a three-dimensional plot of the numerical third overtone solution for an electron in the square box under the influence of a non-central round barrier potential, and the middle figure shows a density plot of the same solution.

In figure 18a we present the probability distribution for the fourth solution of an electron in the square box under the influence of a central square well potential of dimensions (5 ×

$10^{-9}) \times (5 \times 10^{-9})\text{m}^2$ and magnitude 1×10^{-30}J. The solution looks much like the solution of a particle in a box of the dimensions of the well, with some additional leaking into the larger box. These figures show that the program accurately models constant central potentials, such as the central well and the central barrier potential.

In figure 18b we plot the third solution of an electron in the square box under the influence of a non-central square barrier potential with dimensions $(6 \times 10^{-10}) \times (6 \times 10^{-10})\text{m}^2$ and magnitude 1×10^{-18}J, centered around $(x, y) = (5 \times 10^{-9}\text{m}, 2 \times 10^{-9}\text{m})$. These figures show that non-central barrier potentials, too, are modeled well.

Square potential barriers and wells are easy to construct with the code as outlined in section 3.3, since all of the code is based on a Cartesian coordinate system. Round potential wells are, however, preferred as building blocks for muffin-tin potentials. To that end, it is important to check if a round, non-central, barrier or well potential is modeled correctly by the program. Figure 18c shows the third solution of an electron in the square box under the influence of a non-central round barrier potential with radius $(1.1 \times 10^{-11})\text{m}^2$ and magnitude 1×10^{-18}J, centered around $(x, y) = (5 \times 10^{-9}\text{m}, 2 \times 10^{-9}\text{m})$. Comparing figures 18b and 18c, one observes that these systems have very similar solutions, as should be expected. Moreover, closer inspection of these figures shows that the white void at the bottom has a shape that is reminiscent of the shape of the potentials. As the code runs well for these systems, we can confidently construct muffin-tin potentials by summing round, non-central, potentials.

It is important, too, that the code finds the correct eigenvalues corresponding to each eigenfunction. In other words, we want the code to construct the correct energies belonging to each solution of a system. The numerically constructed energies, in fact, correspond well to analytical values. In table 2, two tables with energies are supplied. The left table contains numerical and analytical solutions for the lowest five energy states of an electron in the square two-dimensional box. The second table contains such energies in the case of the previously described two-dimensional harmonic potential. The numerical and analytical values match well for both potentials.

Particle in a Box	
Numerical E_n	Analytical E_n
$7.5270 \times 10^{-5} eV$	$7.5272 \times 10^{-5} eV$
$1.8816 \times 10^{-4} eV$	$1.8818 \times 10^{-4} eV$
$3.0105 \times 10^{-4} eV$	$3.0108 \times 10^{-4} eV$
$3.7425 \times 10^{-4} eV$	$3.7635 \times 10^{-4} eV$
$4.8789 \times 10^{-4} eV$	$4.8926 \times 10^{-4} eV$

Harmonic Potential	
Numerical E_n	Analytical E_n
$9.7536 \times 10^{-4} eV$	$9.7574 \times 10^{-4} eV$
$1.9504 \times 10^{-3} eV$	$1.9514 \times 10^{-3} eV$
$2.9254 \times 10^{-3} eV$	$2.9271 \times 10^{-3} eV$
$3.8998 \times 10^{-3} eV$	$3.9029 \times 10^{-3} eV$
$4.8714 \times 10^{-3} eV$	$4.8786 \times 10^{-3} eV$

Table 2: Comparison between numerical and analytical energies for two-dimensional systems.

The code as outlined in section 3.3 runs well for a number of different potentials, shown in figures 17 and 18, correctly solving for the wave functions and the energies of these systems. With the confidence that the code works well in general, and for round, non-central, barrier and well potentials in particular, the next step is to model indium arsenide systems using muffin-tin approximations.

4.3 Modelling of the Indium Arsenide Chain

In order to examine how well the muffin-tin model approximates the indium arsenide structures of interest in this work, as well as determine which parameters should be used to obtain a good fit, we here model a linear chain of thirty, evenly spaced, indium adatoms, and compare the theoretical results with the empirical results from Pham et al. [24]. Figure 19 shows an STM image of this linear chain.

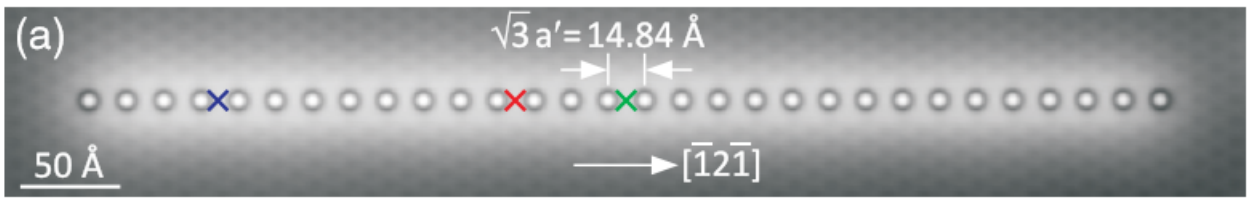

Figure 19: An STM topography image of a linear chain of thirty, evenly spaced, indium adatoms, as found in Pham et al. [24].

The linear chain of thirty, evenly spaced, indium adatoms, which will from now on be referred to as the In_{30} chain, is a relatively simple system. The indium adatoms are spaced $\sqrt{3}a' = 1.484 \times 10^{-9}$ m apart, where $a' = 8.57 \times 10^{-10}$ m is the lattice constant of the 2x2 indium vacancy reconstruction, as shown in figures 8 and 19. The simplicity of the linear chain makes it suitable as a test to calibrate the parameters of the muffin-tin model. Moreover, since the In_{30} chain is a linear chain, the free electrons are tightly confined in the two spatial dimensions orthogonal to the chain, due to the attractive potential of the indium adatoms. This makes all the interesting behaviour essentially one-dimensional. Therefore, the code for one-dimensional simulations, as well as the code for two-dimensional simulations, can be used to model the In_{30} chain.

One-dimensional modeling of the In_{30} chain

In order to model the In_{30} chain in one dimension, the potential of the system is approximated as a sum of simple square wells, each centered around one of the thirty indium adatoms of the chain. At the boundaries, periodic boundary conditions are imposed. The width and depth of the wells are the same for each adatom and, though these parameters are partly determined through trial-and-error, the depth is assumed to be within orders of magnitude of 1 eV, while the width is assumed to be within an order of magnitude of the interatomic spacing of the chain. The ansatz for the depth of the well is based on the charge of the indium adatoms being +1e, while the ansatz for the width derives from the idea that, for the In_{30} chain to be viewed as a single system, the indium adatoms must be able to communicate, and therefore they must not be separated too much.

The muffin-tin potential, as visualised in figure 20, is constructed by summing thirty wells of width 3.2×10^{-9} m and depth 4.8066×10^{-20} J ≈ 0.3 eV at intervals of 1.484×10^{-9} m, which corresponds to the spacing of the adatoms used in Pham et al. [24]. The constructed potential is then shifted down, so that the lowest potential is zero.

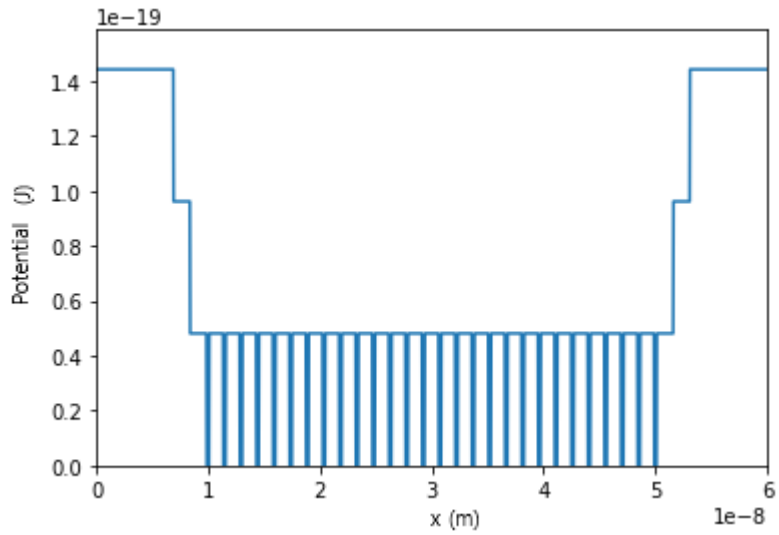

Figure 20: One-dimensional muffin-tin potential used to model the In_{30} chain.

The local density of states of the In_{30} chain as a function of the spatial variable x, including a Lorentzian broadening, discussed in section 3.4, with parameter $\gamma = 5 \times 10^{-23}$, shows clear particle in a box behaviour, as can be seen in figure 21. This is in line with the empirical findings of Pham et al. [24]. The width of the effective box correspond roughly to the length of the In_{30} chain. Next to the system-spanning particle in a box behaviour, the structure of the chain is still evident through the smaller peaks centered on the adatoms, as can be seen in figure 21 ([24], pp. 1-2).

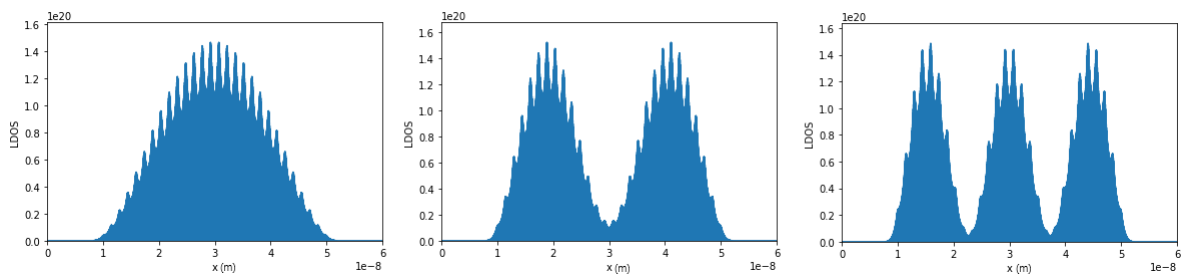

Figure 21: The local density of states of the In_{30} chain for the first three eigenenergies of the system, each as a function of the spatial dimension x of the one-dimensional box. The local density of states is calculated using equation (13), and includes a Lorentzian broadening term with parameter $\gamma = 5 \times 10^{-23}$.

In figure 22a the local density of states is plotted as a function of energy. The curves are calculated using equation (13) with parameter $\gamma = 5 \times 10^{-23}$, for the three spatial coordinates used in Pham et al. [24] (shown in figure 19 by the blue, red, and green crosses). A qualitative agreement between the numerically calculated local density of states in figure 22a and the empirical results in figure 22b can be seen, but a striking difference is observed in the intensity of the numerical and empirical spectra measured at the position of the blue cross. Whereas

the blue line in figure 22a is large for the third, fourth, and fifth peaks, in figure 22b it is very small at those peaks.

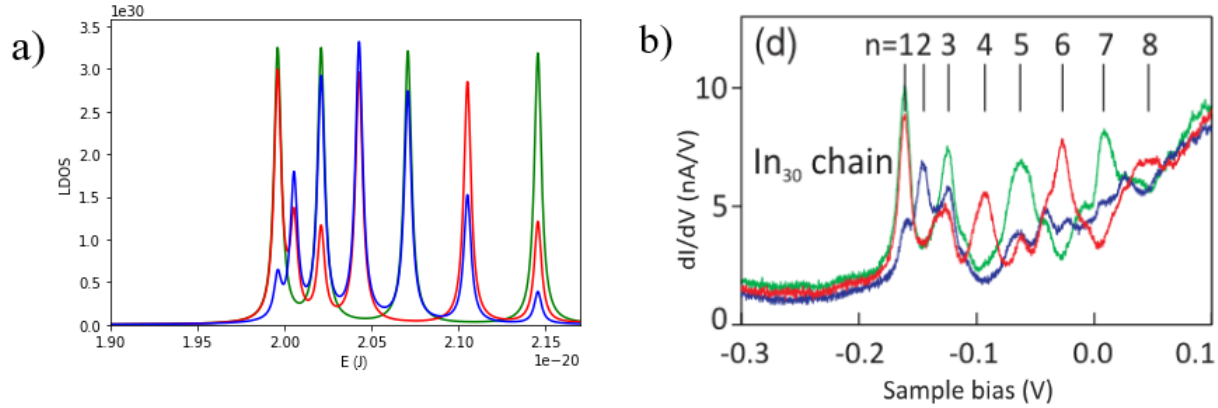

Figure 22: **a)** Numerically constructed local density of states of the In_{30} chain, modeled as a one-dimensional system, as a function of energy. Each colored line corresponds to the position indicated by the crosses of the same color in figure 19.
b) Empirical conductance spectra of the In_{30} chain, measured using an STM. Adapted from Pham et al. [24].

However, the numerical results can reasonably be maintained, as they correspond well to the more detailed results form the supplementary material of Pham et al. [24], shown in figure 23. This figure indicates that blue peaks should be observed for n=3, 4, and 5. On the second page of the supplementary material, Pham et al. [24] also mention that distortion of the measurements may have been caused by defects in the nearby surface region, which could explain the apparent disparity between figures 22a and 22b. ([24], S1)

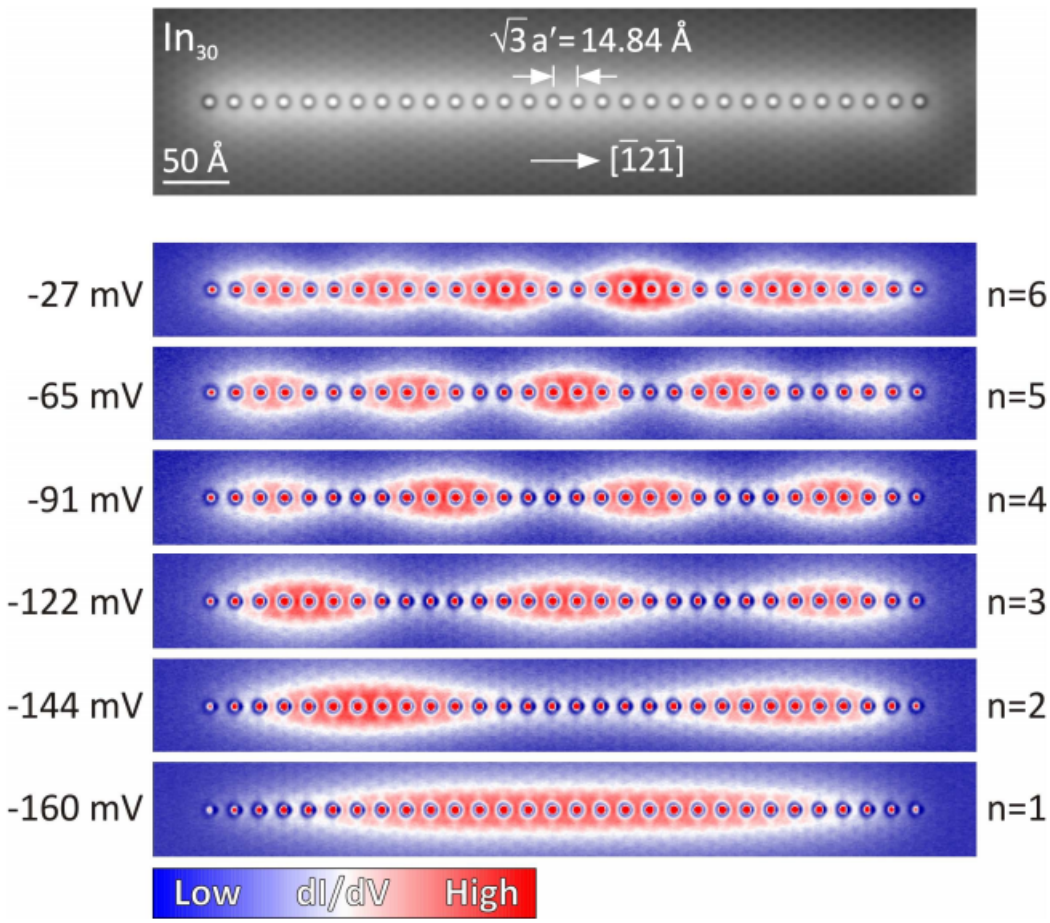

Figure 23: STM images of the In_{30} chain around the first six eigenenergies of the system, as found in figure S1 of the supplementary material of Pham et al. [24].

The energies constructed by the program also match the behaviour of a particle in a box, as can be seen in table 3. In particular, the energies of the In_{30} chain correspond closely to those of an electron in a box of length 4.3930×10^{-8} m, which could have been roughly estimated from figure 20. The energies of the In_{30} chain, listed in table 3, are shifted down by a constant, in order for the first energy levels of the In_{30} chain and the electron in a box to align.

In_{30} chain energies	Particle in a box energies
1.9485×10^{-4} eV	1.9485×10^{-4} eV
7.7941×10^{-4} eV	7.7940×10^{-4} eV
1.7535×10^{-3} eV	1.7537×10^{-3} eV
3.1170×10^{-3} eV	3.1176×10^{-3} eV
4.8696×10^{-3} eV	4.8713×10^{-3} eV

Table 3: Comparison between the numerical energies of the In_{30} chain, modeled in one dimension, and the analytical energies of an electron in a box of length 4.3930×10^{-8} m

.

Two-dimensional modeling of the In_{30} chain

The approach for the modeling of the In_{30} chain in two dimensions is in many ways similar to that of the one-dimensional modeling. A key difference, however, is that the muffin-tin potential will now be defined over two spatial dimensions. This new muffin-tin potential consists of thirty round, evenly spaced, potential wells, each centered on the position of an indium adatom in the In_{30} chain. In particular, each well has a radius of 1.7×10^{-9} m and a depth of 5.7679×10^{-19} J $\approx$ 3.6 eV. These parameters differ from those of the one-dimensional simulation in order to prevent higher energy solutions along the direction orthogonal to the linear chain to appear within the six lowest energy eigenfunctions of the In_{30} chain, as this would be out of line with the empirical results from Pham et al. [24].

A contour plot of the muffin-tin potential constructed in this way is shown in figure 24. Notice that, much like in the one-dimensional case, the potential is at a minimum around the centers of the circles (except the outer two). In other words, the potential is at a minimum around the positions of the indium adatoms in the In_{30} chain.

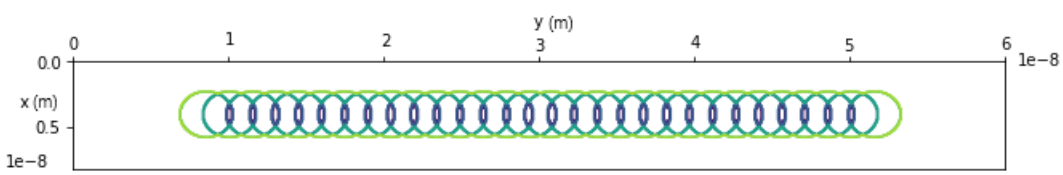

Figure 24: A contour plot of a two-dimensional muffin-tin potential for the In_{30} chain.

This time, however, these areas of minimum potential have a shape that is not at all expected in the physical system. They are elongated in the direction orthogonal to the chain, while being narrow in the direction of the chain, rather than showing a circular symmetry. Though this model is actually not that bad in the case of the In_{30} chain, it breaks down for the more complicated indium arsenide structures discussed later. Another model, which gives better results for the two-dimensional modeling of the In_{30} chain, and is essential for the two-dimensional modeling of the different hexagonal quantum rings, is therefore preferred.

This model is in many ways the same as the one previously described, with the essential difference that the areas of minimum potential, as shown in figure 24, have their potential increased to match the potential of the surrounding, doubly overlapping, round well potential.

A contour plot of the resulting potential is given in figure 25. The modified muffin-tin potential gives results that are closer to the experimental data from Pham et al. [24].

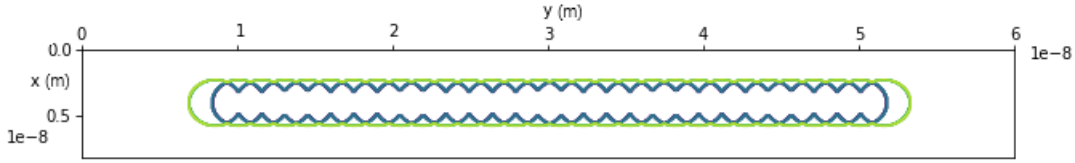

Figure 25: A contour plot of a modified two-dimensional muffin-tin potential for the In_{30} chain.

The numerically constructed solutions for local density of states of the muffin-tin approximation system match well with the empirical findings form Pham et al. [24]. Plotting the local density of states as a function of its spatial coordinates for the first six eigenenergies of the system, results in the right most plots of figure 26. For this two-dimensional model, the Lorentzian broadening parameter in equation (13) is set to $\gamma = 1.5 \times 10^{-21}$. This value is much larger than the one used in the one-dimensional model, which can be explained by considering that, in the one-dimensional model, the free electrons are assumed to be perfectly constrained along the chain, while the two-dimensional model allow for some freedom in one spatial dimension orthogonal to the chain. A comparison of the numerical local density of states to the empirical data from figure S1 of Pham et al. [24], presented on the left of figure 26, shows a qualitatively good agreement.

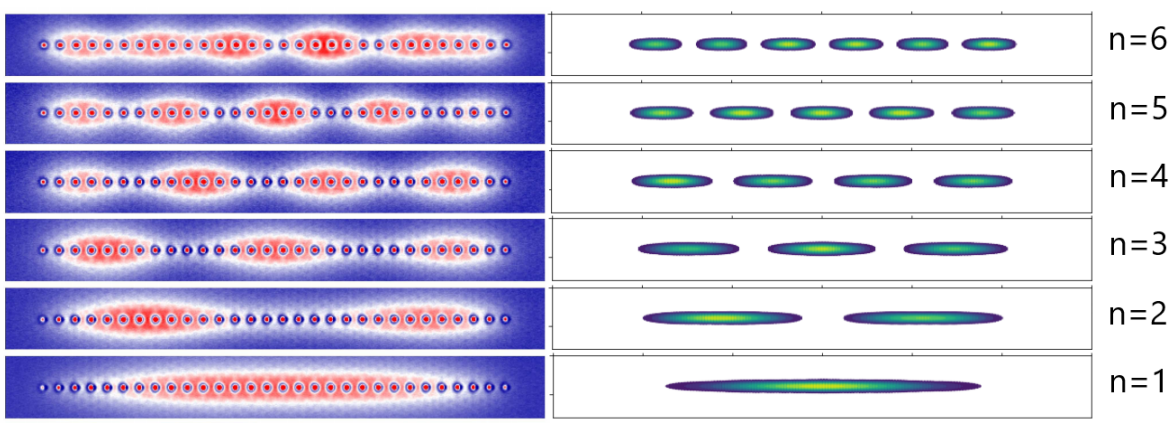

Figure 26: Side-by-side comparison between the measured local density of states of the In_{30} chain on the left, as adapted from the supplementary material of Pham et al. [24], and our calculations of the local density of states of the same chain, using a muffin-tin approximation, on the right.

Plotting the local density of states as a function of energy, for the three positions shown by the blue, red, and green crosses in figure 19, gives a very similar plot as in the one-dimensional model. The numerical local density of states for the In_{30} chain, modeled as a two-dimensional system, again matches well with the empirical data from Pham et al., as

can be seen in figure 27. Though the blue peaks again differ in intensity between figures 27a and 27b, the numerical solutions can be maintained in the light of the excellent fit with the more detailed data shown in figure 26.

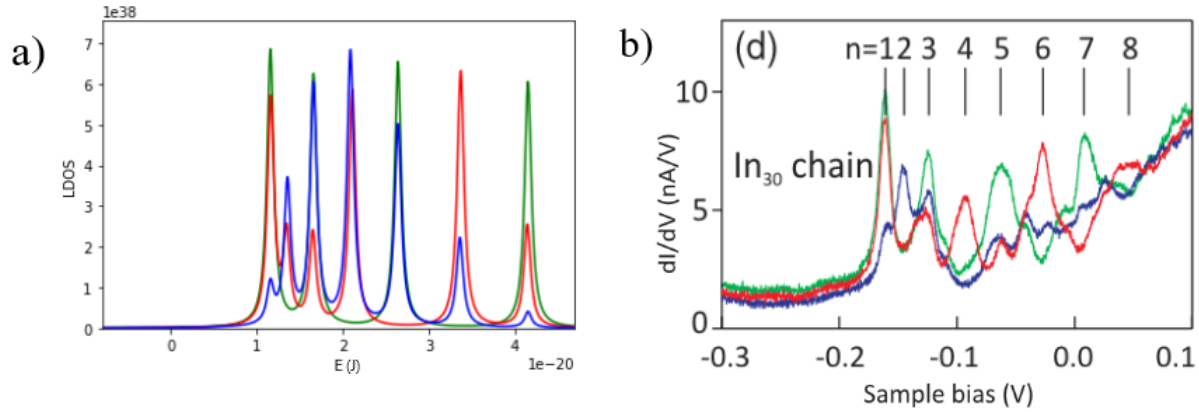

Figure 27: **a)** Numerically constructed local density of states of the In_{30} chain, modeled as a two-dimensional system, as a function of energy. Each colored line corresponds to the position indicated by the crosses of the same color in figure 19.
b) Empirical conductance spectra of the In_{30} chain, measured using an STM. Adapted from Pham et al. [24].

The numerically constructed energies again show particle in a box like behaviour, though with a less perfect fit than in the one-dimensional model. This can potentially be explained by the fact that the two-dimensional muffin-tin potential, shown in figure 25, deviates more from the two-dimensional box in terms of shape, than the one-dimensional muffin-tin potential, shown in figure 20, deviates from the one-dimensional box. In the case of the two-dimensional model, the energies resemble those of an electron in a box of length 4.5×10^{-8} m with an effective electron mass of 4.2385×10^{32} kg. These parameters give a good fit with the empirical data. The energy difference between the first and the seventh peak is 0.187 eV in the numerical simulation, which is close to the approximate 0.170 eV measured in Pham et al. [24]. The numerical energies of the two-dimensional In_{30} chain model, as well as those of an electron in a box of length 4.5×10^{-8} m with an effective electron mass of 4.2385×10^{32} kg, are listed in table 4, to show the clear particle in a box behaviour.

In_{30} chain energies	Particle in a box energies
3.9912×10^{-3} eV	3.9912×10^{-3} eV
1.5965×10^{-2} eV	1.5965×10^{-2} eV
3.4938×10^{-2} eV	3.5920×10^{-2} eV
6.2610×10^{-2} eV	6.3859×10^{-2} eV
9.6319×10^{-2} eV	9.9779×10^{-2} eV

Table 4: Comparison between the numerical energies of the In_{30} chain, modeled in two dimensions, and the analytical energies of an electron in a box of length 4.5×10^{-8} m with an effective electron mass of 4.2385×10^{32} kg.

The data and models above suggest that systems with modified muffin-tin potentials, such as the one shown in figure 25, when treated numerically with the code outlined in section 3.3, show many of the same properties as indium arsenide structures, such as the In_{30} chain. By rearranging the In_{30} chain from a linear chain into a hexagonal ring, we get a system that is interesting in the context of artificial, honeycomb, lattices and graphene.

4.4 Modelling of Hexagonal Quantum Rings

STM patterned indium arsenide hexagonal quantum rings are interesting structures in the context of honeycomb lattices. An STM topography image of the hexagonal quantum ring, consisting of thirty indium adatoms, is shown in figure 28, as found in Pham et al. [24]. A priori, we expect this hexagonal quantum ring to show behaviour much like a circular ring potential. However, when the periodicity of the wave function of the system 'fits' with the hexagonal potential, where the term 'fits' will be substantiated further later, the hexagonal quantum ring shows behaviour that deviates from the circular ring.

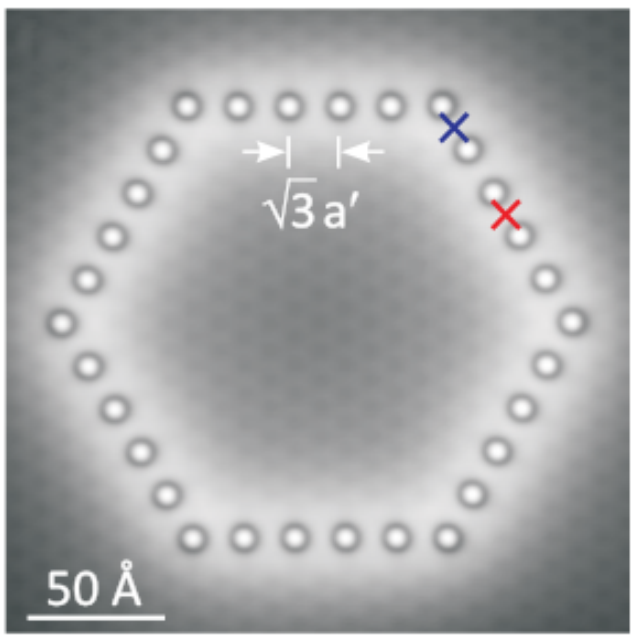

Figure 28: STM topography image of the hexagonal quantum ring, consisting of thirty indium adatoms, as found in Pham et al. [24].

A rough theoretical model for the potential of the hexagonal quantum ring is given by superimposing a perturbation potential of six delta functions, with a hexagonal symmetry, on a circular ring. An example of such a perturbation potential is given in figure 29, as found in the supplementary material of Pham et al. ([24], S4).

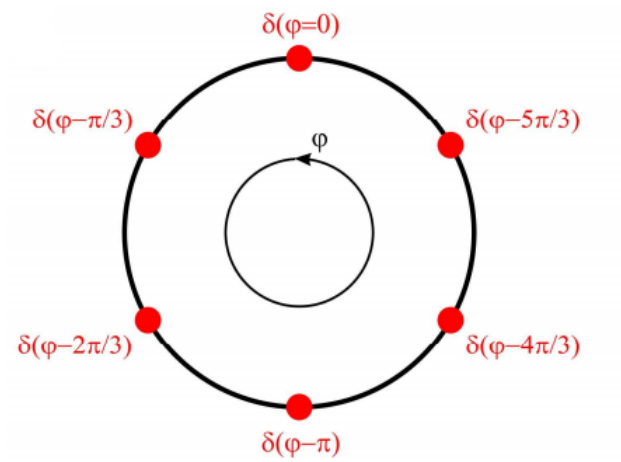

Figure 29: A perturbation potential of six delta functions, arranged with a hexagonal symmetry, on top of a circular ring, as found in the supplementary material of Pham et al. [24].

The perturbation potential due to the six delta functions is given by

$$V_{per}(\varphi) = \sum_{j=0}^{5} \delta\left(\varphi - \frac{j\pi}{3}\right), \tag{14}$$

where φ is the angle shown in figure 29. We treat the hexagonal potential as a perturbation on the circular ring, and take the circular ring eigenstates as an ansatz. In particular, we assume that the probability density solutions of the system shown in figure 29 are proportional to $\rho(\varphi) \propto \cos^2(l\varphi)$, where l is the angular momentum quantum number. Combining equation (14) with this ansatz, the energy contribution of an electron with angular momentum quantum number l, due to the hexagonal perturbation potential, is proportional to

$$U_{per} \propto \int_0^{2\pi} \rho(\varphi - \varphi_0) V(\varphi) d\varphi = \int_0^{2\pi} \left\{ \cos^2\left[l(\varphi - \varphi_0)\right] \sum_{j=0}^{5} \delta\left(\varphi - \frac{j\pi}{3}\right) \right\} d\varphi,$$

which reduces to

$$U_{per} \propto \sum_{j=0}^{5} \cos^2\left[l\left(\frac{j\pi}{3} - \varphi_0\right)\right]. \tag{15}$$

The parameter φ_0 in the above equations represents the phase relation between the probability density and the perturbation potential. Equation (15) has closed solutions of the form

$$\sum_{j=0}^{5} \cos^2\left[l\left(\frac{j\pi}{3} - \varphi_0\right)\right] = \begin{cases} 6\cos^2(l\varphi_0), & \text{if } l = 3n \text{ for } n \in \mathbb{Z}^* \\ 3, & \text{otherwise.} \end{cases} \tag{16}$$

This derivation follows the approach given in the supplementary material of Pham et al. [24].

When calculating the local density of states, solutions with the same energy are summed. Since the energies of the circular ring solutions with quantum numbers $l \notin \{3n \mid n \in \mathbb{Z}^*\}$ are independent of the phase relation φ_0, they are summed over $0 \leq \varphi_0 < 2\pi$. The effect is that the density of states of the $l \notin \{3n \mid n \in \mathbb{Z}^*\}$ solutions is uniform along the ring. These are the ring confined states.

Solutions with quantum numbers $l \in \{3n \mid n \in \mathbb{Z}^*\}$, on the other hand, have energies that are dependent on the phase relation φ_0. Because of this, a degeneracy lifting occurs, so that solutions with a probability density that is localized on the delta potentials have a different energy from those localized between the delta potentials. Any hexagonal model that has an effective difference between the potential at the corners and the edges is expected to show this degeneracy lifting for the $l \in \{3n \mid n \in \mathbb{Z}^*\}$ solutions.

The criterion of the wave function's periodicity 'fitting' that of the hexagonal potential is now defined more precisely as the angular momentum quantum number l being an integer multiple of three. This concept can be understood in a more practical way using figure 30, where the black circle represents the location of the wave function, the red circles represent the locations of the delta potentials, and the radial distance between the blue line and the black circle represents the intensity of the probability density. The larger the radial distance between the blue line and the black circle, the larger the probability density.

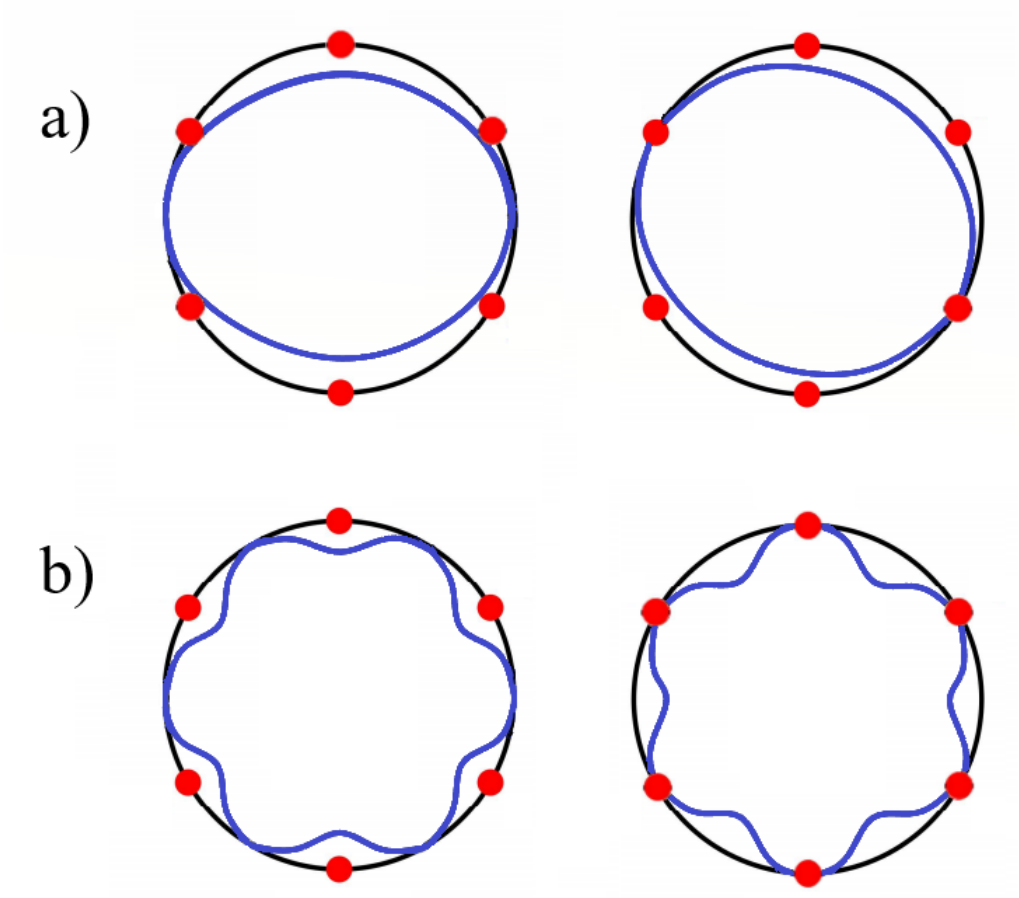

Figure 30: **a)** Two potential configurations of the probability density of the $l = \pm 1$ solutions, with respect to the perturbation potential of figure 29. The black circle represents the position of the wave function, the red dots the positions of the delta potentials, and the radial distance between the blue line and the black circle represents the intensity of the probability density. A larger radial distance between the two corresponds to a larger probability density.
b) Two such configurations for the $l \pm 3$ solutions.

If $|l| = 1$, the probability density will show two maxima and two minima. For different values of φ_0, the maxima will either overlap with two delta potentials at opposite sides of the circle, or each lie in between two such delta potentials. In the first case, the two delta potentials overlapping with the maxima will have a large energy contribution, but the other four delta potentials will contribute little. In the second case, two delta potentials will contribute little or nothing to the energy, but the four other delta potentials will contribute a substantial amount. These effect cancel out exactly for the potential shown in figure 29, so that the energy solutions are independent of the phase relation φ_0. This situation is depicted in figure 30a.

On the other hand, if $|l| = 3$, the probability density has six maxima and six minima. Choosing φ_0 in such a way that each of these maxima overlaps perfectly with a delta potential maximizes the energy contribution of the perturbation potential, while choosing φ_0 in such a way that the delta potentials overlap with the minima of the probability density reduces

the energy contribution to zero. This situation is depicted in figure 30b. Clearly, the choice of the phase relation φ_0 in this case matters for the energy solutions of the system, due to the probability density showing the same kind of symmetry as the perturbation potential.

To test the theoretical model of the hexagonal quantum ring, laid out above, we first model a circular ring with a finite width, in order to test how well the code described in section 3.3 models the upcoming systems. The numerical solutions should show the ring-confined states assumed at the beginning of the theoretical treatment. After that, we model the hexagonal quantum ring as shown in figure 28, using a muffin-tin approximation, to see if these ring-confined states, as well as the degeneracy lifted solutions for $l = 3n$, show up in the numerical solutions. The numerical results are then compared to the empirical results from Pham et al. [24]. Finally, we model two modified hexagonal quantum rings; one with additional indium adatoms at its corners, the other with no corner indium adatoms at all. These last two models are constructed in order to modify the energy gap between the degeneracy lifted $l = 3n$ solutions. The numerical solutions for these systems are again compared to the results from Pham et al. [24].

Modelling of a Circular Potential System

The two-dimensional system with a circular ring potential of radius r and infinitesimal width dr is in many ways the same as a one-dimensional periodic potential of length $2\pi r$. The circular ring model studied here differs from this case in that it has a finite width. Moreover, due to the finite resolution of the numerical resolution, which is defined along Cartesian coordinates, the circular symmetry of the ring studied here is not perfect. Finally, it should be noted that, since only a finite system can be modeled, periodic boundary conditions are imposed at the boundary of the square containing the circular ring model. A contour plot of the circular ring potential is given in figure 31. If the modifications mentioned above do not disrupt the properties of the circular ring too much, the numerical solutions should show the ring-confined states, which are also expected to occur in the hexagonal models.

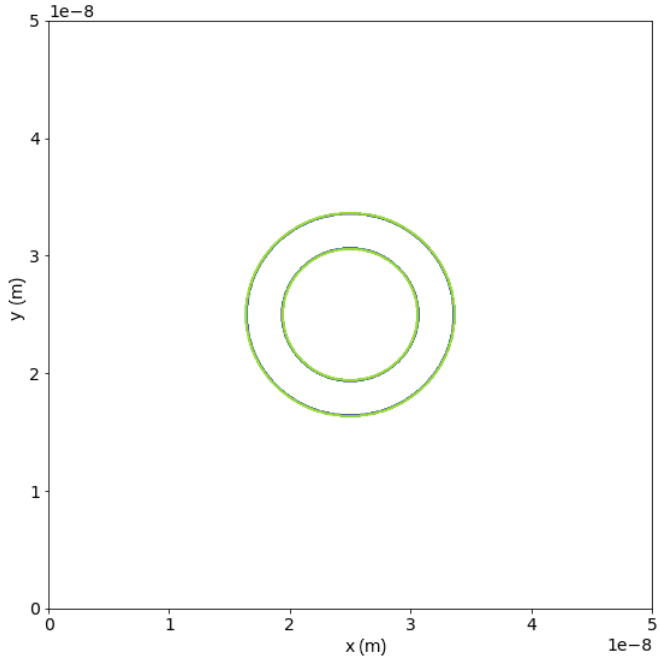

Figure 31: Contour plot of a circular ring potential with inner radius 5.6 nm, outer radius 8.6 nm, and potential -0.12 eV between these two radii.

A plot of the local density of states, calculated including a Lorentzian broadening using equation (13), as a function of its spatial variables for the first eigenenergy of the system is presented in figure 32. The parameter for the Lorentzian broadening is $\gamma = 4 \times 10^{-23}$. Figure 32 shows a clear ring-confined state, confirming the model in figure 31 is a good model for the circular ring.

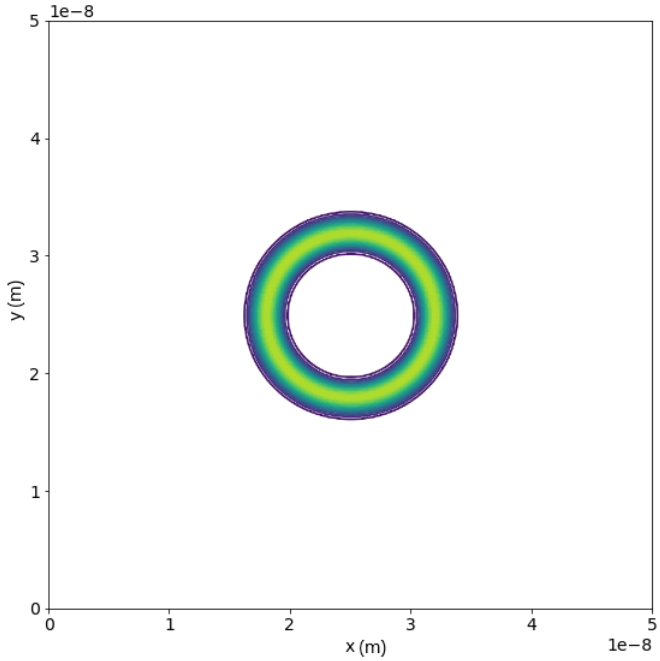

Figure 32: Density plot of the first ring confined state, with $l = 0$, for the circular ring potential shown in figure 31.

For a more detailed analysis, the local density of states is plotted as a function of energy for a given position on the circular ring shown in figure 31. In particular, this position is decided to be $x = y = 3.0 \times 10^{-8}$ m, which lies on a circle of radius $r = 7.1$ nm. A plot of the local density of states, over an energy range containing the first seven eigenenergies of the system, is given in figure 33, which shows clear circular ring behaviour. The energies of the ring have been shifted down by a constant, so that the first ring solution has zero energy, in accordance with the convention of Pham et al. [24]. The first peak, with quantum number $l = 0$, is half as high as the other peaks, because it is the only solution with one, instead of two, allowed angular momentum quantum number values.

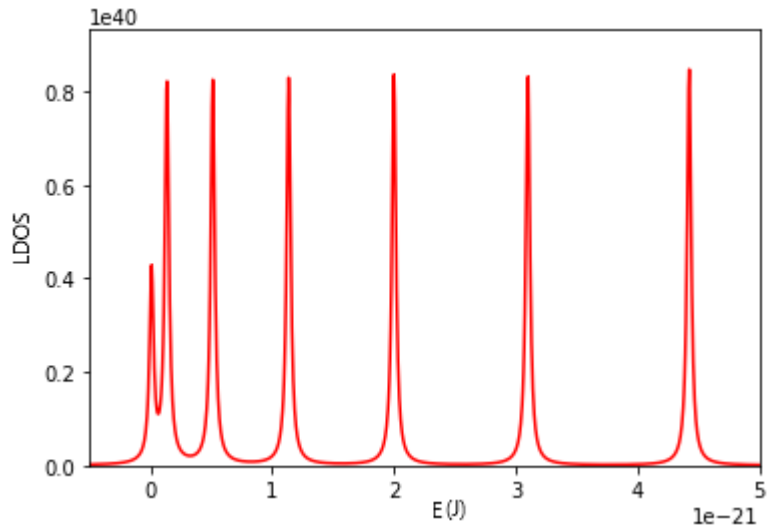

Figure 33: Plot of the local density of states of the circular ring model shown in figure 31, as a function of energy for $x = y = 3.0 \times 10^{-8}$ m.

The numerically constructed energies of the circular ring system of figure 31 closely resemble the analytical energies of a circular ring of radius $r = 6.8130$ nm and infinitesimal width. This radius lies more towards the inner than the outer radius of the circular ring system of figure 31. This can be explained by noting that the energy eigenstates of a circular ring increase quadratically when the radius decreases, so that the inner part of the circular ring dominates the energy of the system. The same mechanism is likely responsible for the noticeable energy differences between the numerical and analytical energies, listed in table 5. Nonetheless, the numerical energies show clear circular ring behaviour.

Numerical circular ring energies	Analytical circular ring energies
0.0 eV	0.0 eV
7.8551×10^{-4} eV	7.8551×10^{-4} eV
3.1346×10^{-3} eV	3.0496×10^{-3} eV
7.0256×10^{-3} eV	6.8616×10^{-3} eV
1.2424×10^{-2} eV	1.2198×10^{-2} eV

Table 5: Comparison between the numerical energies of the circular ring with finite width, shown in figure 31, and the analytical energies of a circular ring of radius $r = 6.8130$ nm with an infinitesimal width.

The program models the circular ring system from figure 31 well, as can be seen by the resemblance between the numerical results for this model and the analytical expectations for a circular ring system with infinitesimal width. With these results as foundation, a hexagonal potential can now be modeled, which can be seen as a perturbation on the circular ring.

Modelling of a Hexagonal Potential System

We now model the hexagonal ring potential with a finite width, as shown in figure 34. The ring-confined solutions should again appear for the angular momentum quantum numbers $l \in \{3n \mid n \in \mathbb{Z}^*\}$. However, when $l = 3n$, the theoretical model, described previously, predicts a degeneracy lifting of the solutions. These non-degenerate states should be observed in the numerical solution of the hexagonal potential system shown in figure 34.

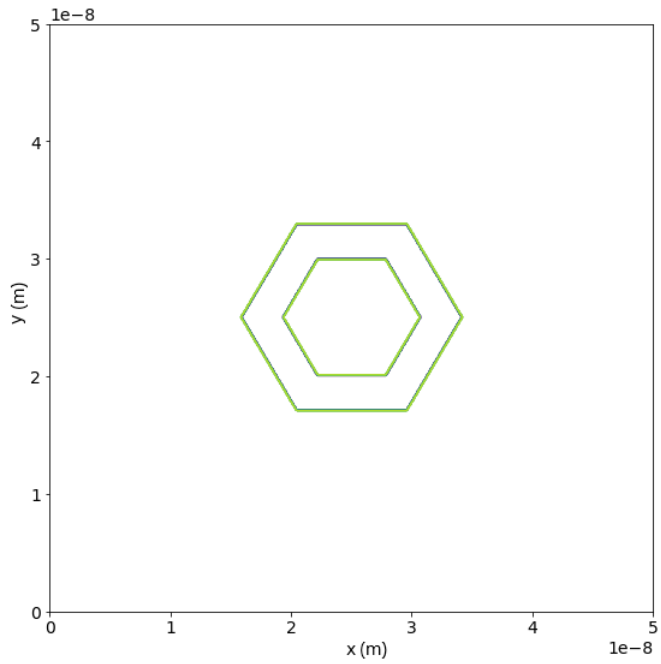

Figure 34: Contour plot of a hexagonal ring potential with the inner hexagon encapsulating a circle of radius 4.9 nm, the outer hexagon encapsulating a circle of radius 7.9 nm, and potential -0.12 eV in between these two hexagons.

Plotting the local density of states, with a Lorentzian broadening $\gamma = 4 \times 10^{-23}$, as a function of its spatial variables, for the first eigenenergy of the system, results in figure 35, which is the ring-confined solution for $l = 0$. The numerical solutions of the system depicted in figure 34 show the desired ring-confined solutions for $l = 0, \pm 1, \pm 2$.

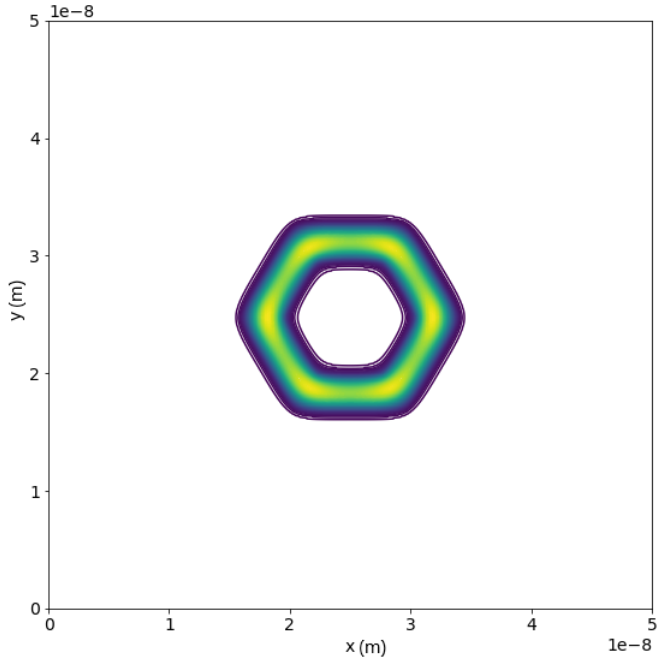

Figure 35: Density plot of the first ring confined state, with $l = 0$, of the hexagonal ring potential shown in figure 34.

To study the local density of states in more detail, we plot it as a function of energy for the two positions indicated by the red and blue crosses in figure 28. The result is given in figure 36. The energies have again been shifted down by a constant, so that the $l = 0$ solution has zero energy. The first three peaks in figure 36 match excellently with the ring-confined states with quantum numbers $l = 0, \pm 1, \pm 2$, indicating that, for these quantum numbers, the hexagonal potential of figure 34 behaves in much the same way as the circular potential of figure 31. However, the third and fourth peak show a behaviour that is very different from the circular ring case. These peaks show the predicted degeneracy lifting for quantum numbers $l = 3n$, which is caused by the matching periodicity of the probability density and the hexagonal potential. More precisely, a probability density that is localized at a corner has a lower energy than a probability density that is localized at an edge, because, due to the finite width of the hexagonal ring in figure 34, there is relatively more attractive potential at the corners than there is at the edges. Solutions with quantum numbers $l = 3n$ are sensitive to their phase relation with respect to the hexagonal ring, so that two distinct solutions emerge; one with the probability density localized at the corners of the hexagon, the other with a probability density predominately on the edges.

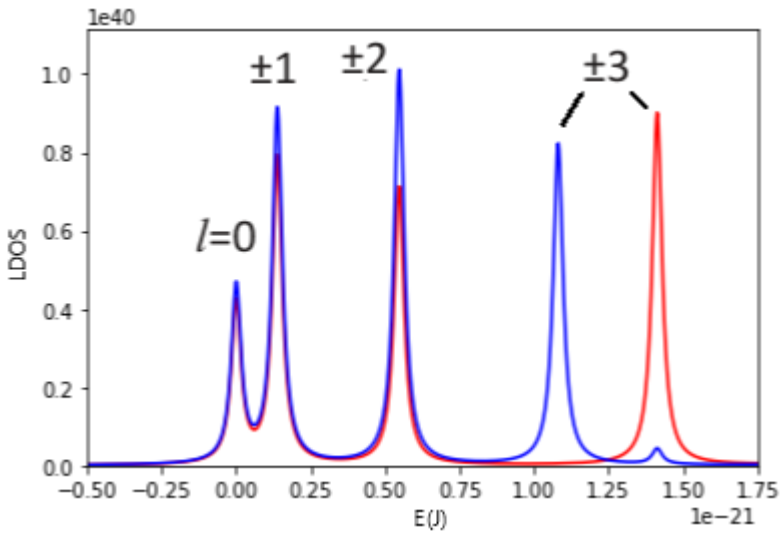

Figure 36: Plot of the local density of states of the hexagonal ring model shown in figure 34, as a function of energy for the positions indicated in figure 28.

Plotting the local density of states as a function of its spatial variables for the energies of the $l = \pm 3$ peaks in figure 36 gives the results shown in figure 37. These figures show a clear localization to either the corners or the edges. The left plot in figure 37 corresponds to the blue $l = \pm 3$ peak in figure 36, while the right plot in figure 37 corresponds to the red $l = \pm 3$ peak. This is in line with the reasoning that there is relatively more attractive potential at the corners of the hexagonal potential, due to the finite width, making the corners effective wells, so that a probability density with peaks at the corners will have a lower energy than one with peaks at the edges.

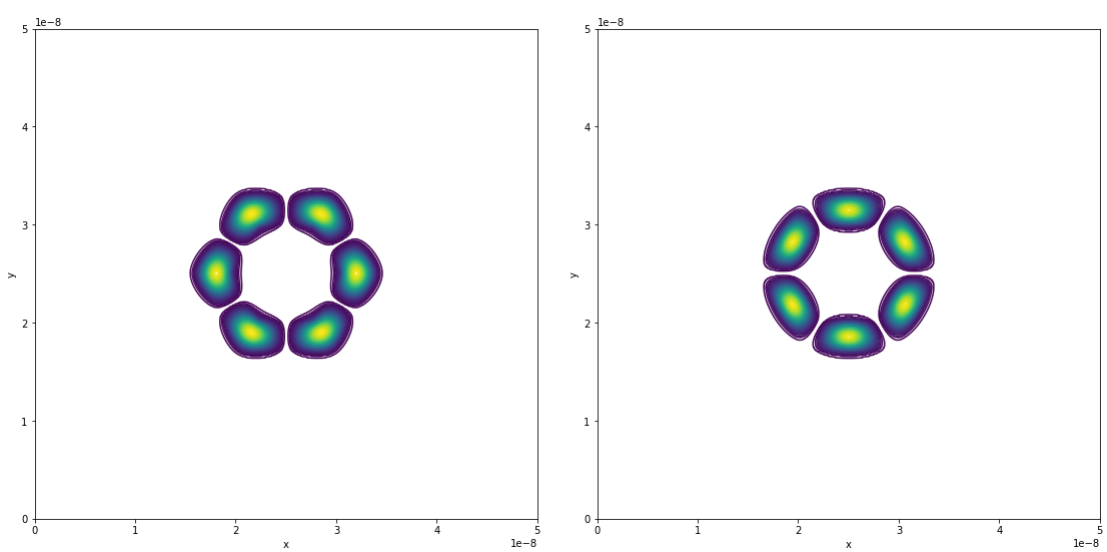

Figure 37: Density plots of the $l = \pm 3$ solutions of the hexagonal ring of figure 34, showing a clear localization to either the corners or the edges.

It is also important to note that the degeneracy lifting behaviour of the $l = \pm 3$ solution is really due to the periodicity of the probability density. This can be seen from figure 38, which is the same as figure 36, but now over a larger energy range. The $l = \pm 4, \pm 5$ peaks show no degeneracy lifting, while the $l = \pm 6$ peaks do. This is precisely in line the with the theoretical predictions laid out above.

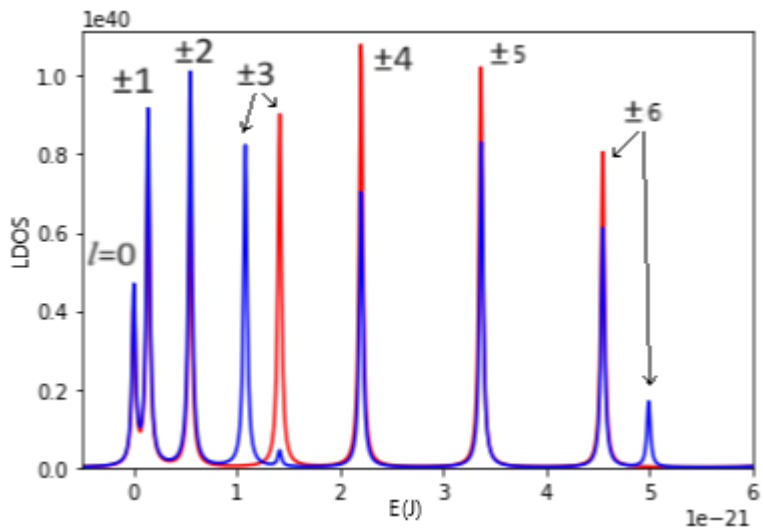

Figure 38: Plot of the local density of states of the hexagonal ring model shown in figure 34, as a function of energy for the positions indicated in figure 28, now over a larger energy range than in figure 36.

The $l = \pm 6$ peaks do not look degeneracy lifted in quite the same way as the $l = \pm 3$ peaks do, but this is due to the choice of the spatial coordinates used to measure the spectra in figure 38. Plotting the local density of states as a function of its spatial variables for $l = \pm 6$, as shown in figure 39, show clearly that the degeneracy lifting of the $l = \pm 6$ peaks is of the same kind as that of the $l = \pm 3$ peaks.

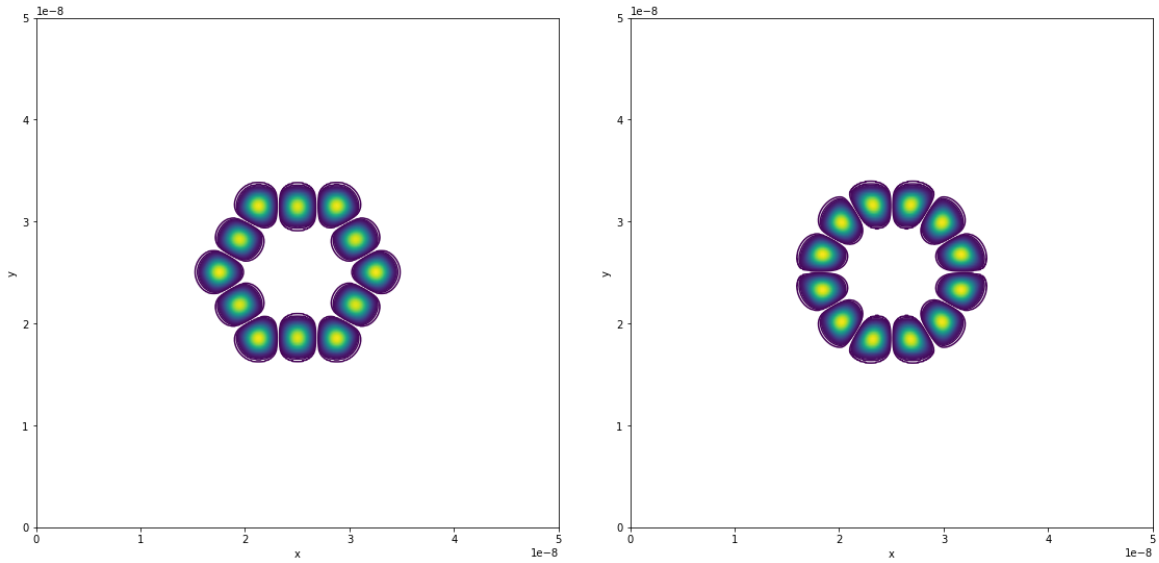

Figure 39: Density plots of the $l = \pm 6$ solutions of the hexagonal ring of figure 34, showing a localization to either the corners or the edges.

The code, laid out in section 3.3, models the hexagonal ring well, and the numerical results confirm the theoretical prediction of degeneracy lifting for angular momentum quantum numbers $l = 3n$ for $n \in \mathbb{Z}^*$. This offers a solid foundation for modeling the hexagonal quantum ring consisting of thirty indium adatoms, shown in figure 28.

Modelling of the In_{30} Hexagonal Quantum Ring

The model of the hexagonal quantum ring differs from the hexagonal potential from figure 34, in that it is a muffin-tin potential, consisting of thirty round potential wells, each centered on the position of an indium adatom, as shown in figure 28. The resulting muffin-tin potential is modified in much the same way as for the In_{30} chain, so that the areas of lowest potential are eliminated. The difference is shown in figure 40. Each well of the muffin-tin potential has a radius of 2.0×10^{-9} m and a depth of 1.9226×10^{-20}J ≈ 0.12 eV. The overall shape of the hexagon was chosen to approximate the quantum ring in figure 28, which results in the inner boundary of the hexagon in figure 40b approximately encapsulating a circle of radius 4.6 nm, while the outer boundary of the hexagon approximately encapsulates a circle of radius 8.2 nm

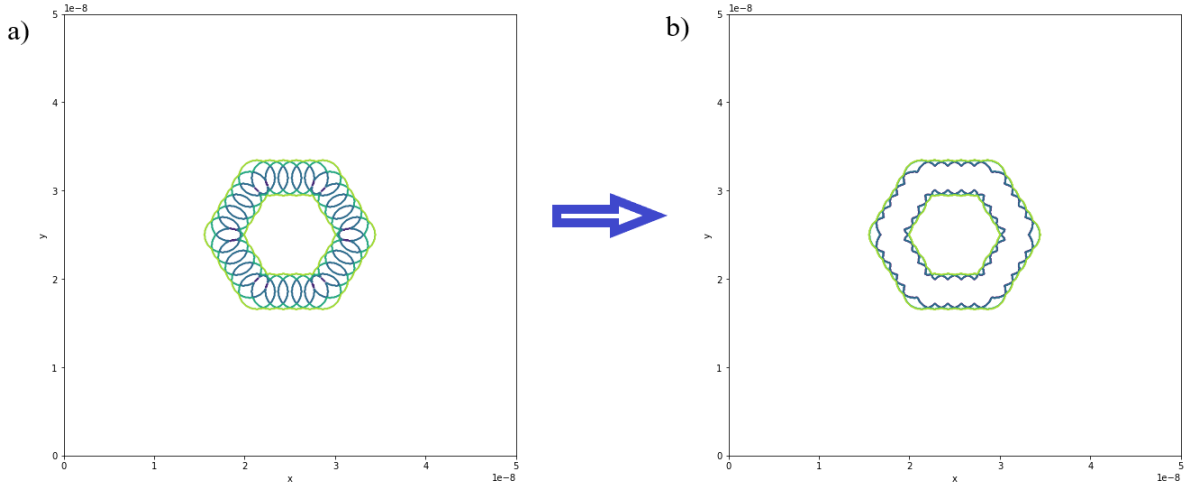

Figure 40: **a)** Contour plot of the simple muffin-tin potential of the hexagonal quantum ring system, shown in figure 28. Notice that the areas with the deepest potential, though centered on the positions of the indium adatoms, should not be part of the modeled potential
b) Contour plot of the modified muffin-tin potential of the hexagonal quantum ring system. The areas with the deepest potential have had their potential elevated to the value of the surrounding potential.

The numerical solution of the system with the muffin-tin potential of figure 40b show many of the same properties as the hexagonal ring system of figure 34.

Plotting the local density of states as a function of its spatial variables, for the eigenenergies corresponding to a number of values of the quantum number l, results in the plots in figure 41. In particular, the plot for $l = 0$ shows that the numerical solutions of the muffin-tin potential shown in figure 40b contain discernible closed-ring solutions. The $l = \pm 3$ plots are there to show that the muffin-tin potential does not simply behave as a circular ring, but rather as a hexagonal ring, with degeneracy lifting for quantum numbers $l = 3n$. The solution for $l = \pm 4$ shows that the degeneracy lifting is specific for the quantum numbers $l = 3n$, so that the $l = \pm 4$ solution shows clear closed-ring behaviour again. Finally, the $l = \pm 6$ solutions show that the behaviour of the $l = \pm 3$ non-degenerate solutions extends to other $l = 3n$ states as well in the numerical simulations, and that this behaviour remains very discernible in the local density of states.

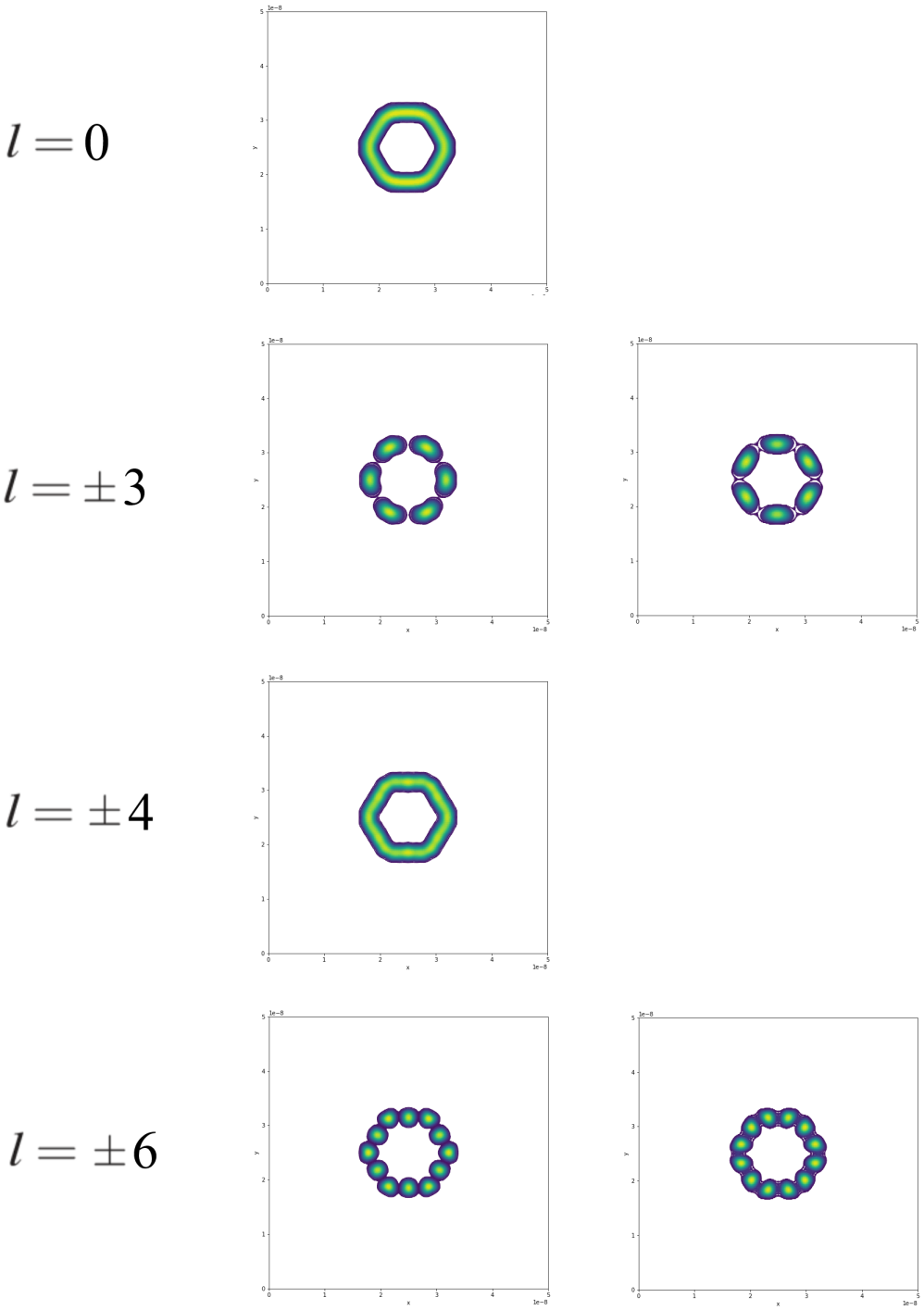

Figure 41: Density plots of the $l = 0, \pm 3, \pm 4, \pm 6$ solutions of the muffin-tin approximation of the hexagonal quantum ring.

The local density of states can also be plotted as a function of energy for the positions indicated by the red and blue crosses in figure 28, see 42. A clear difference between the local density of states of the hexagonal ring, shown in figure 36, and the local density of states shown here, is the spacing between the non-degenerate $l = \pm 3$ peaks. This spacing is much larger for the hexagonal ring. This can be explained by the differences between the potentials shown in figure 40b and 34, specifically the differences at the corners. In the potential of the hexagonal ring, the corners dominate due to the finite width of the ring. On the other hand, for the muffin-tin potential of the hexagonal quantum ring, the corners, though still dominant, are slightly depleted due to the area with the deepest potential not reaching all the way into the corners. Because of this, there is less of an energy difference between the non-degenerate $l = \pm 3$ states in the muffin-tin hexagonal quantum ring model.

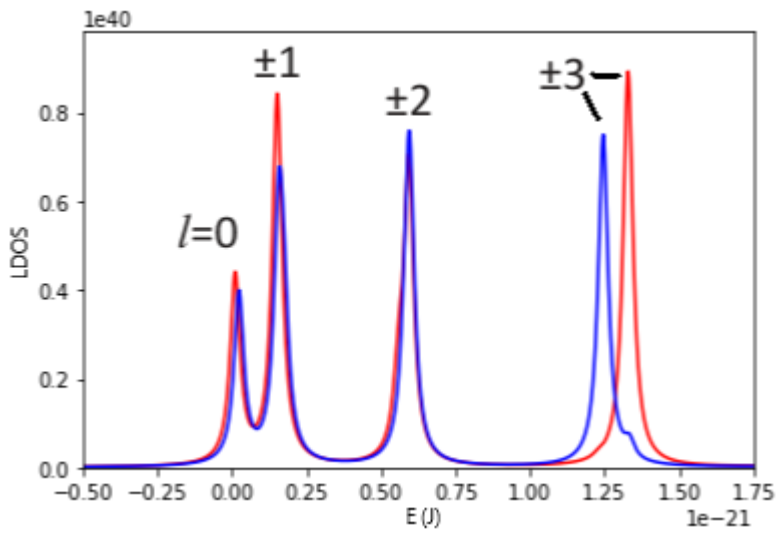

Figure 42: Plot of the local density of states as a function of energy for the muffin-tin potential, shown in figure 40b, which models the hexagonal quantum ring, shown in figure 28. The local density is calculated for the positions indicated in figure 28.

Figure 43 shows the different systems and their corresponding local density of states as a function of energy. The rightmost two figures are empirical measurements from Pham et al. [24]. From the figure, it is clear that the muffin-tin approximation of figure 40b is a better model for the hexagonal quantum ring than the hexagonal ring of figure 34, since the energy difference between the $l = \pm 3$ states is much closer to the empirical data.

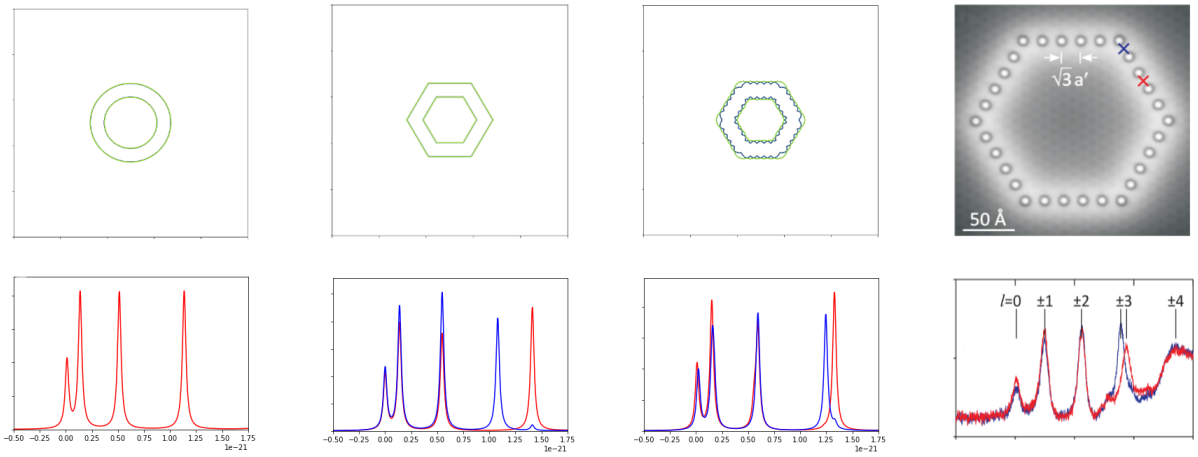

Figure 43: The local density of states as a function of energy, together with the corresponding structure, for, from left to right: A circular ring potential, a hexagonal ring potential, the muffin-tin approximation potential for the hexagonal quantum ring, and the experimentally built hexagonal quantum ring. Note that the two rightmost figures are empirical measurements, both adapted from Pham et al. [24], while all the other figure come from numerical simulations.

The hexagonal quantum ring, consisting of thirty indium adatoms, is modeled excellently by applying the code, laid out in section 3.3, to the modified muffin-tin potential of figure 40b, and the numerical solutions show a behaviour that is much the same as the empirical measurement from Pham et al. [24].

Modelling of the Corner Enhanced In_{36} Hexagonal Quantum Ring

By adding indium adatoms at the corners of the hexagonal quantum ring, the energy splitting of the $l = 3n$ states is enhanced, which should then be visible in the local density of states. This has been experimentally shown by Pham et al. [24], and will be shown numerically here.

The corner enhanced hexagonal quantum ring consisting of thirty six indium adatoms is shown in figure 44, as adapted form Pham et al. [24].

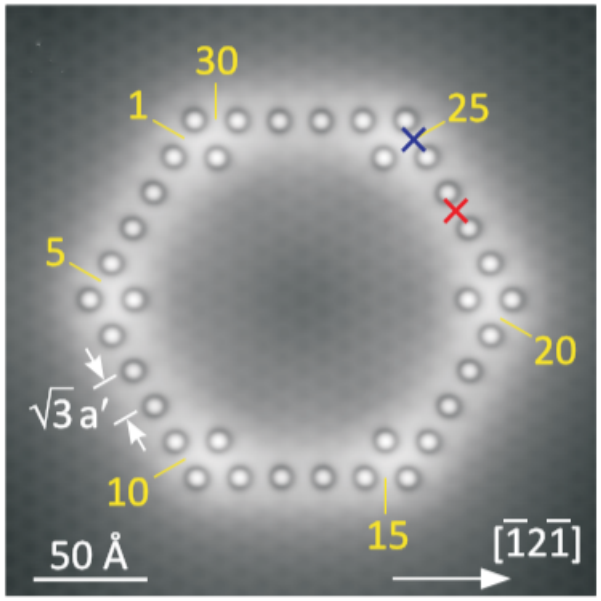

Figure 44: STM topography image of the corner enhanced hexagonal quantum ring consisting of thirty six indium adatoms, adapted from Pham et al. [24].

Figure 45 shows the muffin-tin potential that is used to model this system. Notice that the regions with the deepest potential are, again, eliminated. As intended, the muffin-tin potential shows enhanced potential at the corners.

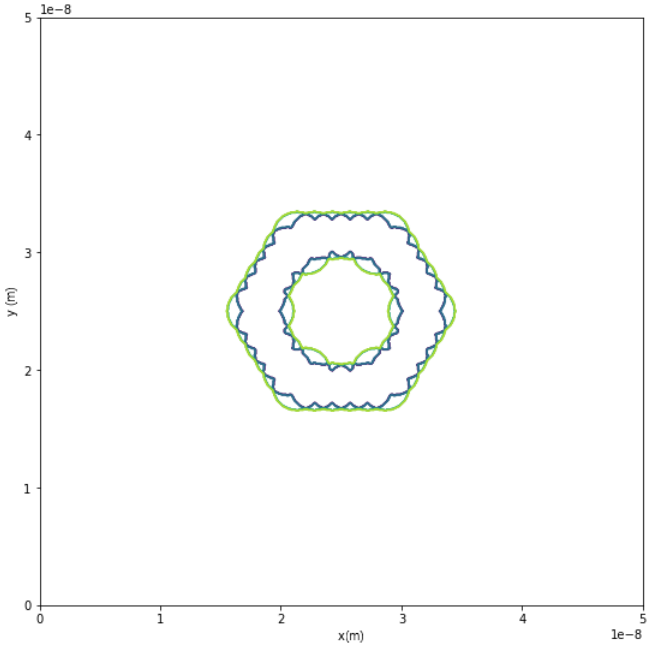

Figure 45: Contour plot of the muffin-tin potential used to approximate the corner enhanced hexagonal quantum ring systems, shown in figure 44.

The numerical solutions of the corner enhanced system, modeled by the muffin-tin potential of figure 45, show clear closed ring solutions for $l = 0, \pm 1, \pm 2$, and manifest degeneracy lifting for $l = \pm 3$, as shown in figure 48. Notice that the localization of the $l = \pm 3$ solutions is stronger than the one seen for the simple hexagonal quantum ring solution, which shows the influence of the enhanced corners.

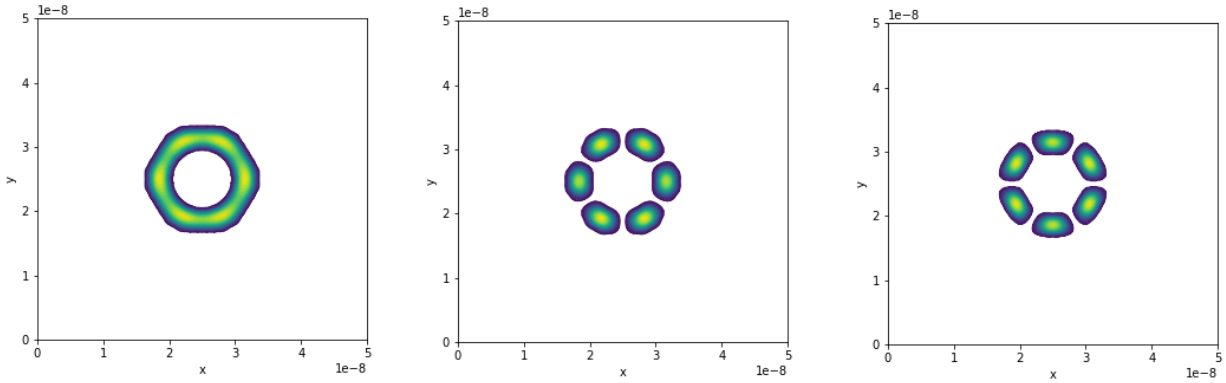

Figure 46: Density plots of the numerical solutions of the muffin-tin potential, shown in figure 45, for $l = 0$ and $l = \pm 3$, respectively.

This enhanced localization of the $l = 3n$ degeneracy lifted states is also clearly observed in experiment. Figure 47 shows a comparison between the experimental spatial conductance maps for the corner enhanced quantum ring, as found in Pham et al. [24], and the numerical solutions of the same system. Both the numerical and the empirical results show that the $l = \pm 3$ states are either strongly localized at the corners or at the edges of the hexagon.

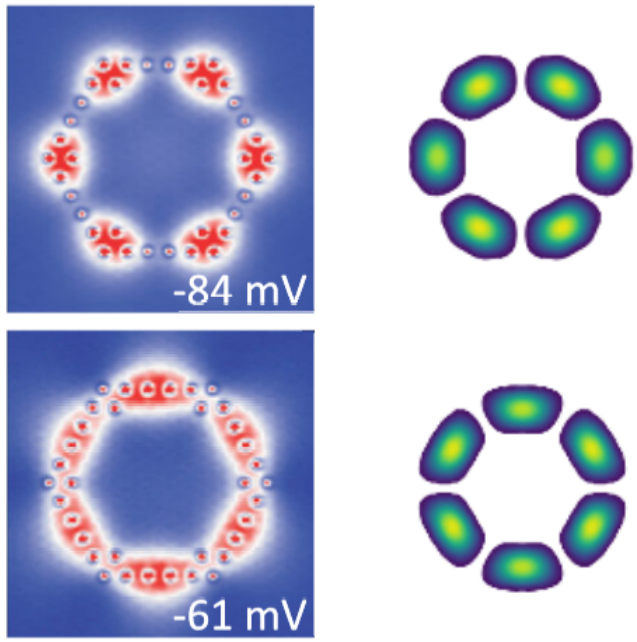

Figure 47: On the left, spatial conductance maps of the corner enhanced quantum ring, as introduced in figure 44, are shown for the $l = \pm 3$ states. On the right, density plots of the numerical solutions of the corner enhanced quantum ring, as modeled by the muffin-tin potential introduced in figure 45, are shown for the same $l = \pm 3$ states.

A plot of the local density of states as a function of energy for the positions indicated by the red and blue crosses in figure 44, is shown in figure 48, where an enhanced energy gap between the $l = \pm 3$ states is visible.

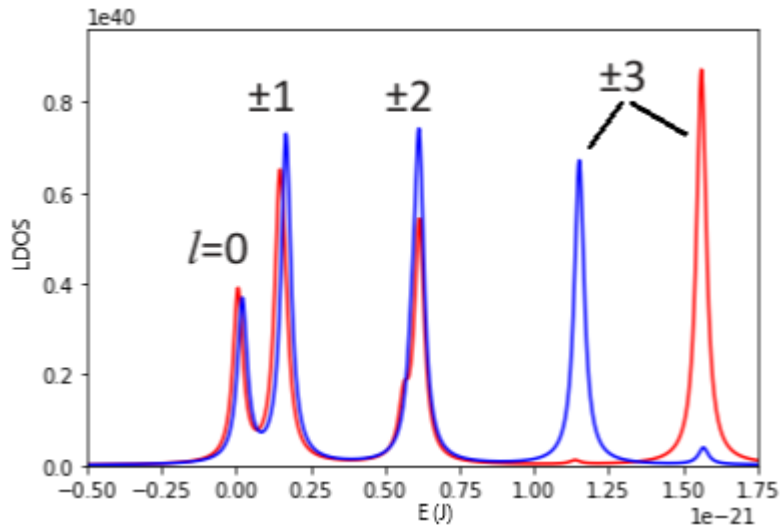

Figure 48: Plot of the local density of states as a function of energy for the muffin-tin potential shown in figure 45, which is used to approximate the corner enhanced hexagonal quantum ring, shown in figure 44. The local density of states is measured at the positions indicated by the red and blue crosses in figure 44. Notice the larger energy gap between the $l = \pm 3$ states, when compared to the local density of states of the simple hexagonal quantum ring, shown in figure 36.

The numerical solutions for the corner enhanced hexagonal quantum ring, modeled using the muffin-tin potential shown in figure 45, shows the same behaviour as the empirical model reported in Pham et al. [24]. This means that the approach to model hexagonal indium arsenide structures, laid out here, is suited for modeling designed hexagonal structures, and probing their properties and behaviour ([24], pp. 2-3).

5 Conclusion

In the context of studying the properties of graphene and, more generally, those of honeycomb lattices, a number of promising artificial lattices, each with its advantages and disadvantages, have been discussed. Molecular graphene, a system of carbon monoxide molecules on copper, can be built at the scale of just a few nanometres with extreme precision and control, due to the individual placement of the carbon monoxide molecules with an STM. This superior control allows for precise variations on the perfect honeycomb lattice, so that the properties of honeycomb lattices can be studied more rigorously. However, the presence of the carbon monoxide molecules on the copper surface also causes an increase in bulk scattering, resulting in a broadening of the conductance spectrum.

Patterned arsenic compounds, such as gallium and indium arsenide, produced using top-down nanofabrication approaches, have the important advantage of scalability. Due to their production method, samples of these patterned arsenic compounds can be created with orders of magnitude more particles than any other artificial lattice approach is capable of. This allows for the study of long-range interactions, many-body effects, as well as spin-orbit interactions. Moreover, type III-V semiconductors, like gallium and indium arsenide, show significantly less screening effects than metals, like copper, and can be produced with much less contamination than real graphene. Patterned arsenic compounds, produced using top-down nanofabrication, are, however, characterised by a relatively large amount of structural disorder, hindering the precise study of honeycomb lattices.

Ultra-cold potassium atoms, trapped in a honeycomb optical lattice, on the other hand, are characterised by no structural disorder at all. Using a setup of interfering laser beams, a highly tunable periodic potential can be created. Such systems are also free from the influence of the rigid structure of solids, and allow for an exceptional control over the nature, strength, and range of inter-particle interactions. In this way, potassium atoms in periodic laser potentials can be used to study regimes, such as ultrastrong spin-orbit coupling and non-Abelian gauge fields, which are currently unreachable in real graphene or any of the artificial lattices. This system, however, lacks the scalability of the arsenic compounds.

STM patterned indium arsenide structures, which are studied more in-depth in this thesis, offer yet another approach to building artificial honeycomb lattices. Combining properties of molecular graphene and top-down nanofabricated arsenic compounds, STM patterned indium arsenide shows great promise as an object of study in the area of artificial honeycomb lattices. It is characterised by the same precision and control that is seen in molecular graphene, due to the individual placement of the indium adatoms using an STM, while retaining the material properties of the arsenic compounds, showing reduced screening effect and providing very pure samples. What it lacks, however, is the scalability of the top-down nanofabricated arsenic compounds. STM patterned indium arsenide structures are well suited as test subjects to study the properties of artificial lattices of patterned arsenic compounds, until production techniques are developed that allow for the creation of large samples of patterned arsenic compounds with little structural disorder.

In section 3, a number of numerical methods are developed, which are capable of modeling both one- and two-dimensional quantum systems. The foundation for these numerical methods is the non-relativistic, time-independent, Schrödinger equation (3). In order to test the numerical methods, in sections 4.1 and 4.2 a number of well known systems in one- and

two-dimensions are modeled, showing that the code works as expected.

The numerical methods use the implicitly restarted Lanczos algorithm to construct the wave functions and energies of quantum systems. This algorithm is very fast, and generally well suited for the large numerical problems treated in this thesis. However, the Lanczos algorithm is not completely stable when the calculations are performed with floating point arithmetic. This causes an unwanted two-fold degeneracy of the eigenvalues. Fortunately, this unwanted degeneracy does not break the model; the numerical methods work well. However, in future work, it is worth considering to look for an algorithm that is not only fast and accurate, but also numerically stable. There has already been done research on this topic ([16], [23], [27], [30]).

In sections 4.3 and 4.4, a number of STM patterned indium arsenide structures are modeled using the numerical methods developed in this thesis, and the results are compared to the empirical results from Pham et al. [24]. The potentials of these systems are approximated using a muffin-tin approximation. The numerical results for the In_{30} chain, modeled both in one- and two-dimensions, show an excellent fit with experimental results. For the potential of the In_{30} chain, modeled in two dimensions, as well as all subsequent systems, a modified muffin-tin potential is used, as shown in figures 25, 40b, and 45.

Subsequently, a theoretical model for the hexagonal quantum ring, as a perturbation on the circular ring, is laid out. This theoretical model is then tested by numerically modeling a circular ring potential, a hexagonal ring potential, and a modified muffin-tin approximation of the hexagonal quantum ring. The results confirm the theoretical model, and match well the experimental results for the hexagonal quantum ring.

Finally, a numerical model of a variation on the hexagonal quantum ring is provided. The corner enhanced In_{36} hexagonal quantum ring, with additional indium adatoms at the corners, is expected to show enhanced degeneracy lifting for $l \in \{3n \mid n \in \mathbb{Z}^*\}$, and this effect is clearly observed, both in numerical simulations and the empirical results from Pham et al. [24].

The numerical methods developed in this thesis give excellent models for elementary quantum systems, as well as muffin-tin approximated STM patterned indium arsenide structures, such as the In_{30} chain, and the hexagonal In_{30} quantum ring. Most importantly, it models the corner enhanced hexagonal In_{36} quantum ring correctly, showing that the code is suited for studying STM patterned indium arsenide structures with setups that vary slightly from the perfect hexagonal structure. The numerical methods developed here can therefore be used to probe the exciting properties and behaviours of artificial honeycomb materials.

References

[1] Bellec, Matthieu, Ulrich Kuhl, Gilles Montambaux, and Fabrice Mortessagne. "Topological Transition of Dirac Points in a Microwave Experiment." *Physical Review Letters* 110, no. 3 (2013).
`https://doi.org/10.1103/physrevlett.110.033902`

[2] Chen, C. Julian. *Introduction to Scanning Tunneling Microscopy*. New York: Oxford University Press, 1993.

[3] Dirac, Paul Adrien Maurice. "Quantum mechanics of many-electron systems." *Proceedings of the Royal Society of London. Series A, Containing Papers of a Mathematical and Physical Character* 123, no. 792 (1929): 714-733.
https://doi.org/10.1098/rspa.1929.0094

[4] Di Liberto, Marco, Tommaso Comparin, Thorge Kock, M. Ölschläger, Andreas Hemmerich, and C. Morais Smith. "Controlling coherence via tuning of the population imbalance in a bipartite optical lattice." *Nature communications* 5, no. 1 (2014): 1-6.
https://doi.org/10.1038/ncomms6735

[5] Di Liberto, Marco, Charles E. Creffield, G. I. Japaridze, and C. Morais Smith. "Quantum simulation of correlated-hopping models with fermions in optical lattices." *Physical Review A* 89, no. 1 (2014): 013624.
https://doi.org/10.1103/PhysRevA.89.013624

[6] Fölsch, Stefan, Jesús Martínez-Blanco, Jianshu Yang, Kiyoshi Kanisawa, and Steven C. Erwin. "Quantum Dots with Single-Atom Precision." *Nature Nanotechnology* 9, no. 7 (2014): 505–508.
https://doi.org/10.1038/nnano.2014.129

[7] Freeney, S. E., J. J. van Den Broeke, AJJ Harsveld van der Veen, I. Swart, and C. Morais Smith. "Edge-dependent topology in Kekulé lattices." *Physical Review Letters* 124, no. 23 (2020): 236404.
https://doi.org/10.1103/PhysRevLett.124.236404

[8] Gardenier, Thomas S., Jette J. Broeke, Jesper R. Moes, Ingmar Swart, Christophe Delerue, Marlou R. Slot, Cristiane Morais Smith, and Daniel Vanmaekelbergh. "p Orbital flat band and Dirac cone in the electronic honeycomb lattice."
arXiv preprint arXiv:2004.03158 (2020).

[9] Gibertini, Marco, Achintya Singha, Vittorio Pellegrini, Marco Polini, Giovanni Vignale, Aron Pinczuk, Loren N. Pfeiffer, and Ken W. West. "Engineering Artificial Graphene in a Two-Dimensional Electron Gas." *Physical Review B* 79, no. 24 (2009).
https://doi.org/10.1103/physrevb.79.241406

[10] Gomes, K., Mar, W., Ko, W. et al. "Designer Dirac fermions and topological phases in molecular graphene". *Nature* 483, 306–310 (2012).
https://doi.org/10.1038/nature10941

[11] Hobson, J. P., and W. A. Nierenberg. "The Statistics of a Two-Dimensional, Hexagonal Net." *Physical Review* 89, no. 3 (1953): 662.
https://doi.org/10.1103/physrev.89.662

[12] Kalesaki, Efterpi, Christophe Delerue, C. Morais Smith, Wouter Beugeling, Guy Allan, and Daniël Vanmaekelbergh. "Dirac cones, topological edge states, and nontrivial flat bands in two-dimensional semiconductors with a honeycomb nanogeometry." *Physical review x* 4, no. 1 (2014): 011010.
https://doi.org/10.1103/PhysRevX.4.011010

[13] Kempkes, S.N., Slot, M.R., Freeney, S.E. et al. "Design and characterization of electrons in a fractal geometry". *Nature Phys* 15, 127–131 (2019).
https://doi.org/10.1038/s41567-018-0328-0

[14] Kempkes, S. N., M. R. Slot, J. J. van Den Broeke, P. Capiod, W. A. Benalcazar, D. Vanmaekelbergh, D. Bercioux, I. Swart, and C. Morais Smith. "Robust zero-energy modes in an electronic higher-order topological insulator." *Nature Materials* 18, no. 12 (2019): 1292-1297.
https://doi.org/10.1038/s41563-019-0483-4

[15] Kevan, S. D. "Evidence for a New Broadening Mechanism in Angle-Resolved Photoemission from Cu(111)." *Physical Review Letters* 50, no. 7 (February 14, 1983): 526–529.
https://doi.org/10.1103/physrevlett.50.526

[16] Lanczos, C. "An Iteration Method for the Solution of the Eigenvalue Problem of Linear Differential and Integral Operators." *Journal of Research of the National Bureau of Standards* 45, no. 4 (October 1950): 255–282.
https://doi.org/10.6028/jres.045.026

[17] Laughlin, R.B. "Graphene Density of States." stanford.edu, May 19, 2008.
http://large.stanford.edu/courses/2008/ph373/laughlin2/

[18] Lehoucq, Richard B., Danny C. Sorensen, and Chao Yang. *ARPACK Users Guide: Solution of Large-Scale Eigenvalue Problems with Implicitly Restarted Arnoldi Methods.* Philadelphia: SIAM, 1998.
https://doi.org/10.1137/1.9780898719628

[19] Lühmann, Dirk-Sören, Kai Bongs, Klaus Sengstock, and Daniela Pfannkuche. "Self-trapping of bosons and fermions in optical lattices." *Physical review letters* 101, no. 5 (2008): 050402.
https://doi.org/10.1103/PhysRevLett.101.050402

[20] Martínez-Blanco, Jesús, Steven C. Erwin, Kiyoshi Kanisawa, and Stefan Fölsch. "Energy Splitting of Image States Induced by the Surface Potential Corrugation of InAs(111)A." *Physical Review B* 92, no. 11 (2015): 115444.
https://doi.org/10.1103/physrevb.92.115444

[21] Novoselov, Kostya S., Andre K. Geim, Sergei V. Morozov, D. Jiang, Y. Zhang, Sergey V. Dubonos, Irina V. Grigorieva, and Alexandr A. Firsov. "Electric field effect in atomically thin carbon films." *science* 306, no. 5696 (2004): 666-669.
10.1126/science.1102896

[22] Novoselov, Kostya S., Andre K. Geim, Sergei Vladimirovich Morozov, Da Jiang, Michail I. Katsnelson, IVa Grigorieva, SVb Dubonos, and and AA Firsov. "Two-dimensional gas of massless Dirac fermions in graphene." *nature* 438, no. 7065 (2005): 197-200.
https://doi.org/10.1038/nature04233

[23] Paige, C. C. "Computational Variants of the Lanczos Method for the Eigenproblem." *IMA Journal of Applied Mathematics* 10, no. 3 (1972): 373–381.
https://doi.org/10.1093/imamat/10.3.373

[24] Pham, Van Dong, Kiyoshi Kanisawa, and Stefan Fölsch. "Quantum Rings Engineered by Atom Manipulation." *Physical Review Letters* 123, no. 6 (August 6, 2019).
https://doi.org/10.1103/physrevlett.123.066801

[25] Polini, Marco, Francisco Guinea, Maciej Lewenstein, Hari C. Manoharan, and Vittorio Pellegrini. "Artificial Honeycomb Lattices for Electrons, Atoms and Photons." *Nature Nanotechnology* 8, no. 9 (2013): 625–633.
https://doi.org/10.1038/nnano.2013.161

[26] Reich, Eugenie Samuel. "Graphene Knock-Offs Probe Ultrafast Electronics." *Nature* 497, no. 7450 (May 22, 2013): 422–423.
https://doi.org/10.1038/497422a

[27] Saad, Yousef. *Numerical Methods for Large Eigenvalue Problems.* 2nd ed. Manchester University Press, 2011.
https://doi.org/10.1137/1.9781611970739

[28] Slot, M., Gardenier, T., Jacobse, P. et al. "Experimental realization and characterization of an electronic Lieb lattice." *Nature Phys* 13, 672–676 (2017).
https://doi.org/10.1038/nphys4105

[29] Slot, M. R., S. N. Kempkes, E. J. Knol, W. M. J. Van Weerdenburg, J. J. Van Den Broeke, D. Wegner, D. Vanmaekelbergh, A. A. Khajetoorians, C. Morais Smith, and I. Swart. "p-Band engineering in artificial electronic lattices." *Physical Review X* 9, no. 1 (2019): 011009.
https://doi.org/10.1103/PhysRevX.9.011009

[30] Sorensen, Danny C. "Implicitly restarted Arnoldi/Lanczos methods for large scale eigenvalue calculations." *Parallel Numerical Algorithms.* Springer, Dordrecht, (1997): 119-165.
https://doi.org/10.1007/978-94-011-5412-3_5

[31] Tarruell, Leticia, Daniel Greif, Thomas Uehlinger, Gregor Jotzu, and Tilman Esslinger. "Creating, Moving and Merging Dirac Points with a Fermi Gas in a Tunable Honeycomb Lattice." *Nature* 483, no. 7389 (2012): 302–305.
https://doi.org/10.1038/nature10871

[32] Tkachenko, O. A., V. A. Tkachenko, I. S. Terekhov, and O. P. Sushkov. "Effects of Coulomb Screening and Disorder on an Artificial Graphene Based on Nanopatterned Semiconductor." *2D Materials* 2, no. 1 (2015): 014010.
https://doi.org/10.1088/2053-1583/2/1/014010

[33] Vergés, J. A., and E. Louis. "Electron States on the (111) Surface of Copper." *Solid State Communications* 22, no. 10 (June 1977): 663–666.
https://doi.org/10.1016/0038-1098(77)90792-X